

1 Cloud response to co-condensation of water and organic vapors over the boreal 2 forest

3
4 Liine Heikkinen^{1,2}, Daniel G. Partridge³, Sara Blichner^{1,2}, Wei Huang⁴, Rahul Ranjan^{1,2}, Paul
5 Bowen³, Emanuele Tovazzi³, Tuukka Petäjä⁴, Claudia Mohr^{1,2}, and Ilona Riipinen^{1,2}

6 ¹Department of Environmental Science (ACES), Stockholm University, Stockholm, Sweden

7 ²Bolin Centre for Climate Research, Stockholm University, Stockholm, Sweden

8 ³Department of Mathematics and Statistics, Faculty of Environment, Science and Economy, University of Exeter,
9 Exeter, United Kingdom

10 ⁴Institute for Atmospheric and Earth System Research (INAR) / Physics, University of Helsinki, Helsinki, Finland

11
12 *Correspondence to:* Liine Heikkinen (liine.heikkinen@aces.su.se) and Ilona Riipinen (ilona.riipinen@aces.su.se)

13 Abstract

14 Accounting for the condensation of organic vapors along with water vapor (co-condensation) has been shown in
15 adiabatic cloud parcel model (CPM) simulations to enhance the number of aerosol particles that activate to form
16 cloud droplets. The boreal forest is an important source of biogenic organic vapors, but the role of these vapors in
17 co-condensation has not been systematically investigated. In this work, the environmental conditions under which
18 strong co-condensation -driven cloud droplet number enhancements would be expected over the boreal biome are
19 identified. Recent measurement technology, specifically the Filter Inlet for Gases and AEROSols (FIGAERO)
20 coupled to an iodide-adduct Chemical Ionization Mass Spectrometer (I-CIMS), is utilized to construct a volatility
21 distribution of the boreal atmospheric organics. Then, a suite of CPM simulations initialized with a comprehensive
22 set of concurrent aerosol observations collected in the boreal forest of Finland during Spring 2014 is performed.
23 The degree to which co-condensation impacts droplet formation in the model is shown to be dependent on the
24 initialization of temperature, relative humidity, updraft velocity, aerosol size distribution, organic vapor
25 concentration and the volatility distribution. The predicted median enhancements in cloud droplet number
26 concentration (CDNC) due to accounting for the co-condensation of water and organics fall on average between
27 16 and 22%. This corresponds to activating particles 10–16 nm smaller in dry diameter, that would otherwise
28 remain as interstitial aerosol. The highest CDNC enhancements (Δ CDNC) are predicted in the presence of a
29 nascent ultrafine aerosol mode with a geometric mean diameter of ~40 nm and no clear Hoppel minimum,
30 indicative of pristine environments with a source of ultrafine particles (e.g., via new particle formation processes).
31 Such aerosol size distributions are observed 30–40% of the time in the studied boreal forest environment in spring
32 and fall when new particle formation frequency is the highest. Five years of UK Earth System Model (UKESM1)
33 simulations are further used to evaluate the frequencies to which such distributions are experienced by an Earth
34 System Model over the whole boreal biome. The frequencies are substantially lower than those observed at the
35 boreal forest measurement site (<6% of the time) and the positive values, peaking in spring, are modeled only
36 over Fennoscandia and western parts of Siberia. Overall, the similarities in the size distributions between observed
37 and modeled (UKESM1) are limited, which would limit the ability of this model, or any model with a similar
38 aerosol representation, to project the climate-relevance of co-condensation. For the critical aerosol size
39 distribution regime, Δ CDNC is shown to be sensitive to the concentrations of semi-volatile and some
40 intermediate-volatility organic compounds (SVOCs and IVOCs) especially when the overall particle surface area
41 is low. The magnitudes of Δ CDNC remain less affected by the more volatile vapors such as formic acid and
42 extremely low and low volatility organic compounds (ELVOCs and LVOCs). The reasons for this are that most

43 volatile organic vapors condense inefficiently due to their high volatility below cloud base and the concentrations
44 of LVOCs and ELVOCs are too low to gain significant concentrations of soluble mass to reduce critical
45 supersaturations enough for droplet activation to occur. Reduction of the critical supersaturation caused by organic
46 condensation emerges as the main driver of the modeled Δ CDNC. The results highlight the potential significance
47 of co-condensation in pristine boreal environments close to sources of fresh ultrafine particles. For accurate
48 predictions of co-condensation effects on CDNC, also in larger scale models, an accurate representation of the
49 aerosol size distribution is critical. Further studies targeted at finding observational evidence and constraints for
50 co-condensation in the field are encouraged.

51

52 **1 Introduction**

53 Boreal forests emit significant quantities of volatile organic compounds (VOCs, Guenther et al., 1995; Artaxo et
54 al., 2022), such as monoterpenes, that undergo oxidation in the atmosphere. The condensable oxidation products
55 contribute considerably to the secondary organic aerosol (SOA) mass concentrations in the boreal forest air (e.g.,
56 Tunved et al., 2006; Artaxo et al., 2022). The emissions of monoterpenes are strongly temperature-dependent,
57 which leads – together with the higher oxidative potential in the sunlit months – to highest biogenic SOA
58 concentrations in summer (Paasonen et al., 2013; Heikkinen et al., 2020; Mikhailov et al., 2017). This has recently
59 been shown to have implications for cloud properties above the boreal forest through the availability of more
60 cloud condensation nuclei (CCN; Yli-Juuti et al., 2021; Petäjä et al., 2022; Paasonen et al., 2013). Under constant
61 meteorological conditions in the boreal forest, an increase in aerosol concentration typically results in an increase
62 in cloud droplet number concentration (CDNC) and smaller average droplet size for a given liquid water content
63 (Yli-Juuti et al., 2021). These effects alter the cloud brightness making clouds scatter incoming solar radiation
64 more efficiently (Twomey effect; Twomey, 1974, 1977). The relationships between the number of aerosol
65 particles, CDNC, and their effects on climate are, however, non-linear and complex, which makes aerosol-cloud
66 interactions the largest source of uncertainty in radiative forcing estimates from climate models (e.g., Lohmann
67 and Feichter, 2005; Carslaw et al., 2013; Bellouin et al., 2020). The development of “bottom-up” predictive
68 models is needed for providing accurate, yet robust, simplifications of key processes involved in aerosol-cloud
69 interactions – eventually for inclusion in climate models in computationally efficient parameterizations.

70 Numerous studies have been carried out to understand the role of condensable organic vapors in SOA
71 formation (e.g., Hallquist et al., 2009; Shrivastava et al., 2017) and hence the concentrations of CCN (i.e. particles
72 of at least 50–100 nm in diameter for the water vapor supersaturations typical of the boreal environments; Cerully
73 et al., 2011; Sihto et al., 2011; Paramonov et al., 2013; Hong et al., 2014; Paramonov et al., 2015). The yields of
74 volatile, intermediate-volatility or semi-volatile organic compounds (VOCs, IVOCs, or SVOCs) from
75 monoterpene oxidation, such as those of pinonaldehyde, formic acid, or acetic acid, are generally much higher
76 than those of the readily condensable lower-volatility vapors (low-volatility organic compounds, LVOCs and
77 extremely low volatility organic compounds, ELVOCs), but they are typically not considered directly important
78 for SOA or CCN formation. The above-mentioned volatility classes are determined based on the volatilities of
79 individual compounds binned into a volatility basis set (VBS; Donahue et al., 2006): VOCs have a saturation
80 vapor concentration (C^* ; given in units of $\mu\text{g m}^{-3}$ throughout the paper) of at least $10^7 \mu\text{g m}^{-3}$, IVOCs are distributed
81 in the C^* range of $[10^3, 10^6] \mu\text{g m}^{-3}$, SVOCs of $[1, 100]$, LVOCs of $[10^{-3}, 10^{-1}]$ and ELVOCs have a C^* below $10^$

82 ⁴ $\mu\text{g m}^{-3}$ (e.g., Donahue et al., 2011). While VOCs, IVOCs, and some SVOCs are unlikely to produce significant
83 concentrations of SOA at ground level without additional oxidation steps or multiphase chemistry, some of them
84 can condense at higher altitudes if transported aloft (e.g., Murphy et al., 2015). In addition, aerosol liquid water
85 plays a key role in determining the amount of SVOCs and IVOCs in the condensed phase. Liquid water acts as an
86 absorptive medium, and a higher liquid water content can enable a higher quantity of organic vapors to partition
87 into the condensed phase. However, the role of water in determining partitioning coefficients is often neglected
88 when absorptive partitioning theory (Pankow et al., 2001) is applied. Barley et al. (2009) demonstrated that the
89 inclusion of water, when predicting absorptive partitioning using Raoult's law, could lead to evident increases in
90 organic aerosol (OA) mass concentrations under atmospherically relevant OA loadings. Later work by Topping
91 and McFiggans (2012) showed how under a decreasing temperature trend, the concentration of aerosol liquid
92 water increases making the solution particle more dilute enabling enhanced dynamic partitioning of organic vapors
93 (together with water vapor). This work focuses on the dynamic SVOC and IVOC condensation together with
94 water vapor (co-condensation) in rising and cooling air motions, and the effects co-condensation poses on cloud
95 microphysics.

96 Warm (liquid) clouds can form when air rises and cools, eventually leading to the air being supersaturated
97 with water vapor. The excess water vapor condenses onto aerosol particles, rapidly growing them into cloud
98 droplets. While water represents the most abundant vapor in the atmosphere, also other trace species can influence
99 the cloud droplet activation process as the cooling of the rising air triggers also their condensation. The partitioning
100 of these other vapors is partially driven by the decrease in temperature itself, which makes the species less volatile,
101 but more important it is the increase in aerosol liquid water, and the dilution of the aerosol solution that enables
102 them to partition to the liquid phase (Topping and McFiggans, 2012). As the trace vapors condense in the rising
103 air under sub-saturated conditions, the molar fraction of water in the swelling aerosol particles increases slower
104 than in the absence of this co-condensation process, which in turn leads to the condensation of additional water
105 by the time the air parcel reaches lifting condensation level. The co-condensation of water with other trace vapors
106 eventually leads to a reduction in critical supersaturation (s^*) required for droplet activation of the particles due to
107 an increased amount of organic solute (Topping and McFiggans, 2012), as described by Köhler theory (Köhler,
108 1936). Topping et al. (2013) studied the impact of organic co-condensation on CDNC using a cloud parcel model
109 (CPM) initialized with a suite of realistic conditions describing the aerosol particle number size distribution
110 (PNSD), composition, and OA volatility distribution. They showed significant enhancements in CDNC (ΔCDNC
111 up to roughly 50%) when comparing simulations with organic condensation (CC) to simulations without it
112 (noCC). In addition to co-condensing organics and water, also co-condensation of nitric acid and ammonia
113 together with water has been suggested to enhance CDNC in earlier process modeling studies (e.g., Kulmala et
114 al., 1993; Korhonen et al., 1996; Hegg, 2000; Romakkaniemi et al., 2005). Direct experimental studies of co-
115 condensation remain challenging, however, as aerosol particles are typically dried during the sampling process
116 and the loss of liquid water may lead to evaporation of co-condensed organics, too. While direct observational
117 evidence of co-condensation is scarce, recent laboratory studies show significant water uptake due to co-
118 condensation of propylene glycol and water onto ammonium sulfate particles (Hu et al., 2018). In addition,
119 ambient observations from Delhi and Beijing suggest co-condensation of hydrochloric acid (HCl) or nitric acid
120 (HNO_3) with water vapor, respectively, to be of essence in reproducing particle hygroscopicities corresponding
121 to the visibility measurements during haze events (Gunthe et al., 2021; Wang et al., 2020).

122 The cloud response to co-condensation in the form of Δ CDNC has been previously shown to result from
123 the complex interplay between updraft velocity, PNSD and organic compound volatility distribution (Topping et
124 al., 2013). For the same amount of organic vapor, Topping et al. (2013) modelled a non-linear updraft response
125 of Δ CDNC. The highest Δ CDNC were obtained when updrafts were below 1 m s^{-1} , but the peak Δ CDNC was
126 dependent on the initial PNSD characteristics. Under higher updrafts, the modelled Δ CDNC was found to decrease
127 exponentially as a function of updraft, but the plateau of the curve depended on the initial PNSD – although the
128 dependence on the exact parameters describing multimodal PNSD were not extensively explored. If assumed
129 representative of the global continents, Δ CDNC values of tens of percent could impose a significant impact on
130 predictions of cloud albedo and the Earth's radiative budget. In fact, Topping et al. (2013) suggest accounting for
131 co-condensation could result in up to 2.5% increase in cloud albedo (corresponding to global Δ CDNC = 40%).
132 This albedo increase would translate into a -1.8 W m^{-2} change in the global cloud radiative effect over land.
133 Topping et al. (2013) stress, however, that the impacts of co-condensation will be spatially heterogeneous because
134 of variable surface albedo and variation in VOC sources. For comparison, one should note that the net radiative
135 effect of clouds is approximately -20 W m^{-2} (Boucher et al., 2013). The recent best estimate of the effective
136 radiative forcing from aerosol-cloud interactions is, on the other hand, $-1.0 [-1.7 \text{ to } -0.3] \text{ W m}^{-2}$ (Forster et al.,
137 2021). The potential contribution of co-condensation to estimates of radiative forcing due to aerosol–cloud–
138 climate feedbacks remains unclear.

139 Boreal forests make up about one third of the Earth's forested area, which makes the boreal biome an
140 important source of biogenic organic vapors that could affect droplet activation in warm clouds through co-
141 condensation. Δ CDNC due to co-condensation over the boreal forest could reduce the albedo over the dark boreal
142 forest canopy. In a warming climate, temperature-dependent biogenic terpene emissions (Guenther et al., 1993)
143 are expected to rise (e.g., Turnock et al., 2020). These increasing emissions enrich the ambient pool of organics
144 available for condensation in rising air. As suggested in Topping et al. (2013), through the effects organic co-
145 condensation poses on CDNC, organic co-condensation could enhance the proposed negative climate feedback
146 mechanism associated with the biogenic SOA (Kulmala et al., 2004; Spracklen et al., 2008; Kulmala et al., 2014;
147 Yli-Juuti et al., 2021), the magnitude of which is currently highly uncertain (Thornhill et al., 2021; Sporre et al.,
148 2019; Scott et al., 2018; Paasonen et al., 2013; Sporre et al., 2020).

149 Since the publication of the Topping et al. (2013) study, improved constraints of the effective volatilities
150 of organic aerosol (e.g., Thornton et al., 2020) are available through the application of chemical ionization mass
151 spectrometers (CIMS) providing molecular level information on gas- and particle-phase composition in near-real
152 time. With the up-to-date volatility parameterizations using the molecular formulae retrieved from CIMS data,
153 volatility distributions can be calculated along a volatility scale ranging from ELVOCs to VOCs, while previous
154 techniques could not enable constraints on volatilities exceeding $C^* = 1000 \mu\text{g m}^{-3}$ (Cappa and Jimenez, 2010).
155 This means that a notable amount of semi- and intermediate volatility vapors with high co-condensation potential
156 were not included in the early organic co-condensation work (Topping et al., 2013; Crooks et al., 2018). The
157 recent methodological developments motivate revisiting work of Topping et al. (2013), as potentially large
158 concentrations of condensable organic vapors have been so far neglected.

159 In this study, the cloud response to the co-condensation of organic vapors over the boreal forest of
160 Finland is investigated using a CPM. Measurements and parameterization techniques involving FIGAERO-I-
161 CIMS data are utilized to constrain the volatility distribution of organics for these simulations. In addition, to

162 ensure realistic modeling scenarios, simultaneously recorded measurements of PNSD and chemical composition
163 from the Aerosol Chemical Speciation Monitor (ACSM) are used for the CPM initialization. 97 unique CPM
164 simulations are performed, initialized with conditions from boreal spring and early summer following
165 measurement time series recorded during the Biogenic Aerosols – Effects on Clouds and Climate (BAECC)
166 campaign at the Station Measuring Atmosphere–Ecosystem Relationships (SMEAR) II (Hari and Kulmala, 2005)
167 in Finland (Petäjä et al., 2016) and the sensitivity to meteorological conditions is studied. These simulations are
168 then used to characterize the environmental conditions (with respect to the size distribution and organic aerosol
169 volatility distribution characteristics) that promote co-condensation-driven CDNC enhancements in the boreal
170 atmosphere. The frequencies to which a strong cloud response to co-condensation could be expected and its
171 potential spatiotemporal variability over the boreal biome is further investigated using long-term measurements
172 from SMEAR II station and UK Earth System Model (UKESM1) simulations.

173 **2 Methods and data**

174 This section covers the description of the main modeling tools and measurement data used in this work involving
175 the description of the CPM utilized (Sect. 2.1), the CPM initialization and simulation setup (Sect. 2.2.), and CPM
176 input data measurements and data processing, with independent sections dedicated to the retrievals of volatility
177 distributions for atmospheric organics (Sect. 2.3 and subsections therein). The final section is dedicated for
178 describing the UKESM1 simulations (Sect. 2.4).

179

180 **2.1 The adiabatic cloud parcel model (PARSEC-UFO)**

181 The base of the CPM chosen for this study is the Pseudo-Adiabatic bin-micRophySics university of Exeter Cloud
182 parcel model (PARSEC). It was developed based on the Institute for Marine and Atmospheric research Utrecht
183 (IMAU) pseudo-adiabatic CPM (ICPM, Roelofs and Jongen, 2004; Roelofs, 1992) to allow for simulation of both
184 pseudo-adiabatic and adiabatic ascents of air parcels (Partridge et al., 2011, 2012) as well as numerous
185 optimizations to reduce simulation computational costs, such as a variable time-stepping scheme option for the
186 dynamics/microphysics. PARSEC simulates the condensation and evaporation of water vapor on aerosol particles,
187 particle activation to cloud droplet, unstable growth, collision and coalescence between droplets, and entrainment.
188 In all simulations performed in this study PARSEC is used in adiabatic ascent configuration and the fixed time-
189 stepping option in PARSEC is employed.

190 The model can be initialized with aerosol populations consisting of one or more internal or external
191 mixtures of sulfuric acid, ammonium bisulfate, ammonium sulfate, OA, black carbon, mineral dust and sea salt.
192 The PNSD are presented in a moving-center binned microphysics scheme comprising 400 size bins between 2 nm
193 and 5 μm in dry radii, which are constructed at model initialization from the three parameters describing log-
194 normal size distributions for the i number of modes – the geometric mean diameter (D_i), the total mode number
195 concentration (N_i), and the geometric standard deviation (σ_i). The model can be initialized with up to four log-
196 normal aerosol modes. PARSEC further provides time evolutions of key thermodynamic and microphysical
197 parameters e.g., the air parcel temperature (T), pressure (p), supersaturation (s), altitude (z) and the aerosol particle
198 and hydrometeor size distributions.

199 The dynamical equations used in PARSEC to simulate the adiabatically ascending air parcel equations
200 are the same to those presented by Lee and Pruppacher (1977), where the vertical parcel displacements are
201 determined by the updraft velocity (w , set to a fixed positive constant value in the PARSEC simulations):

$$\frac{dz}{dt} = w. \quad (1)$$

202 The changes in pressure are calculated assuming hydrostatic balance and the temperature decrease along the ascent
 203 follows the dry adiabatic lapse rate while also accounting for the latent heat release due to condensation:

$$-\frac{dT}{dt} = \frac{gw}{c_{p,a}} + \frac{L_e}{c_{p,a}} \frac{dx_v}{dt} + \mu_J \left[\frac{L_e}{c_{p,a}} (x_v - x'_v) + (T - T') \right] w \quad (2)$$

204 where g is the acceleration of gravity, L_e the latent heat of evaporation, $c_{p,a}$ the specific heat capacity of air and x_v
 205 the water vapor mixing ratio of the air parcel. μ_J is the entrainment rate describing mixing of parcel air with
 206 environmental air characterized with x'_v and T' . The water vapor mixing ratio in the air parcel changes with the
 207 evolving ambient supersaturation:

$$\frac{ds}{dt} = \frac{p}{\varepsilon e_s} \frac{dx_v}{dt} - (1 + s) \left[\frac{\varepsilon L_e}{R_a T^2} \frac{dT}{dt} + \frac{g}{R_a T} w \right], \quad (3)$$

208 where $\varepsilon = R_w/R_v = M_w/M_a = 0.622$ i.e., the ratio between the specific gas constants for air and water vapor,
 209 respectively, or alternatively the molecular weight of water and air, respectively. e_s is the saturation vapor pressure
 210 of water. To solve the ordinary differential equations (Eqs. 2–3), the time derivative of the water vapor mixing is
 211 approximated as

$$\frac{dx_v}{dt} \approx -\frac{\Delta x_L}{\Delta t} - \mu_J (x_v - x'_v + x_L) w \quad (4)$$

212 where Δt is the model time step (0.1 seconds) and the liquid water mixing ratio (x_L) is calculated as a sum of the
 213 liquid water mixing ratio across all the 400 size bins (index i) for each assigned mode composition (index j):

$$\Delta x_L = \frac{4\pi\rho_w}{3\rho_a} \sum_{i=1}^{n_a} \sum_{j=1}^{n_b} n_{ij} (r_{ij}^3 - r_{ij, \text{dry}}^3), \quad (5)$$

214 where ρ_w is density of water, ρ_a is the density of dry air, n_{ij} is the number of particles within size bin i and
 215 composition j , and finally r_{ij} and $r_{ij, \text{dry}}$ are the wet and dry radii of the particles, respectively. The wet radii and
 216 hence also the particle masses (m) change as water condenses onto the particle (indices dropped for simplicity):

$$\frac{dm}{dt} = 4\pi\rho_w r^2 \frac{dr}{dt} = \frac{4\pi\rho_w r (S - S_{\text{eq}})}{\frac{\rho_w RT}{\text{DIFF}_v^* e_s} + \frac{L_e \rho_w}{kT} \left(\frac{L_e}{RT} - 1 \right)}, \quad (6)$$

217 where k is the thermal conductivity of air, and DIFF_v^* is size-dependent water vapor diffusivity (from Pruppacher
 218 and Klett, 1997). Eq. (6) is approximated within PARSEC using a linearized form of the condensation equation
 219 (Hänel, 1987). Finally, S is the ambient saturation ratio ($S = s + 1$) and S_{eq} ($S_{\text{eq}} = \text{RH} / 100\%$) the equilibrium
 220 saturation ratio over the (spherical) wet particle surface, the difference of which determines the quantity of excess
 221 vapor for the diffusional growth of the particle. While S depends on the updraft source and condensation sink (Eq.
 222 3), S_{eq} depends on the particle wet radius and composition and it can be calculated using the Köhler equation
 223 (Köhler, 1936), traditionally expressed as:

$$S_{\text{eq}} = \frac{e}{e_s} = a_w \exp\left(\frac{2M_w \gamma}{RT \rho_w r}\right) \quad (7)$$

224 where e is the partial vapor pressure of water in equilibrium, a_w the water activity, γ the droplet surface tension
 225 (assumed to be that of water; see Table 1), R the universal gas constant, T the droplet temperature and r the droplet

226 radius. Assuming dilute droplets, Eq. 7 is approximated in PARSEC as follows for the equilibrium supersaturation
 227 ratio (Hänel, 1987):

$$S_{\text{eq}} \approx \exp \left(\frac{A}{r} - \frac{B}{\left(\frac{r}{r_{\text{dry}}} \right)^3 - 1} \right), \quad (8)$$

228 where

$$A = \frac{2M_w \gamma}{RT\rho_w} \quad (9)$$

229 and

$$B = \frac{\phi_s M_w \varepsilon_V \rho_s \nu}{M_s \rho_w} \quad (10)$$

230 A and B in Eqs. (9) and (10) are the Köhler coefficients, where M_w is the molecular weight of water (g mol^{-1}), M_s
 231 refers to the molar mass of the soluble fraction, ρ_w is the density of water (g m^{-3}), ϕ_s is the osmotic coefficient
 232 of salt in the solution ($\phi_s \approx 1$ in ideal solutions), ν is the dissociation constant, and ρ_s and ε_V are the density and
 233 the volume fraction of the soluble mass in the aerosol particle, respectively. The dissociation constant is calculated
 234 as $\nu = (\sum_i c_i^+ + \sum_j c_j^-) / \sum_{ij} c_{ij}$, where, c_i^+ and c_j^- are the concentrations of positive and negative ions and c_{ij}
 235 is the concentration (mol L^{-1}) of the electrolytes in solution. For detailed descriptions of the B term, the reader is
 236 directed to Roelofs (1992).

237 PARSEC has been further extended to include Köhler and condensation/evaporation equations
 238 for organic species of varying volatilities (Lowe, 2020). This extension of the model is referred to as PARSEC
 239 with the Unified Framework for Organics (PARSEC-UFO), and it is the CPM version used throughout the
 240 presented study. Within PARSEC-UFO, the volatility distributions are given using the VBS framework (Donahue
 241 et al., 2006) with q volatility bins – each assigned with a different saturation vapor concentration, C^* . The
 242 condensation/evaporation equation for organic species is described in the same manner as in Topping et al. (2013)
 243 and as shown for water vapor in Eq (6):

$$\frac{dm_q}{dt} = \frac{4\pi \rho_w r \text{DIFF}_g^* (S_q - S_{\text{eq},q}) e_{s,q}}{\frac{\text{DIFF}_g^* \Delta H_{\text{vap},q} S_{\text{eq},q} e_{s,q} \rho_q}{\lambda T} \left(\frac{\Delta H_{\text{vap},q}}{R_{v,q} T} - 1 \right) + \rho_q R_{v,q} T} \quad (11)$$

244 where DIFF_g^* is the gas phase diffusivity (see details in Topping et al., 2013 supplementary information), and λ is
 245 the heat conductivity of air. Both DIFF_g^* and λ are corrected for the transition regime of condensation. $\Delta H_{\text{vap},q}$ is
 246 the enthalpy of vaporization, $e_{s,q}$ the saturation vapor pressure, $S_{\text{eq},q}$ the equilibrium saturation ratio and ρ_q the
 247 density of organic species in the q^{th} volatility bin. $S_{\text{eq},q}$ is calculated analogous to the Köhler equation (Eq. 8):

$$S_{\text{eq},q} = a_q \exp \left(\frac{2v_q \gamma}{RT r} \right) \quad (12)$$

249 where a_q is the activity of q^{th} volatility bin in the bulk condensed phase, which equals the molar fraction of q due
 250 to the ideal solution approach of the study, and v_q is the molar volume of q . Following the organic condensation,
 251 the Köhler B term (Eq. 10) is updated along the adiabatic ascent, which impacts S_{eq} for water and thereby its

252 condensation. Finally, as temperature decreases along the parcel's adiabatic ascent, the reductions in C^* are
 253 accounted for using an Arrhenius-type Clausius-Clapeyron relation:

$$C^* = C^*(T_{\text{ref}}) \exp\left(\frac{\Delta H_{\text{vap}}}{R} \left(\frac{1}{T_{\text{ref}}} - \frac{1}{T}\right)\right), \quad (13)$$

254 where R is the universal gas constant and T is the air parcel's ambient temperature in Kelvin, and T_{ref} is 298.15 K.
 255 The $C^*(T_{\text{ref}})$ are calculated within PARSEC-UFO using the initial conditions as reference. ΔH_{vap} remain constant
 256 throughout the simulations in this study, and are not C^* -dependent for simplicity. It should be noted that the time
 257 step of 0.1 seconds can be too high for solving Eq. (11) for the highest volatility bins. For instance, during
 258 condensation the model may encounter $m_q + \frac{dm_q}{dt} < 0$.

259 If this happens then the condensation step is rejected, and instead condensation happens with a temporary timestep
 260 of $dt/2$ across two iterations. This ensures non-negative m_q . We should stress, that this sub-timestep is a new
 261 feature unique to PARSEC-UFO which is different to the variable time-stepping scheme option available in
 262 PARSEC.

263

264

265 2.2 PARSEC-UFO initialization and simulation setup

266 The simulations shown within this work are performed with PARSEC-UFO with or without co-condensation.
 267 Initially, before the start of the adiabatic ascent, an initialization takes place in PARSEC-UFO. This involves the
 268 calculation of the binned wet particle number size distribution and in the case, where co-condensation is enabled,
 269 the initialization of the volatility distribution of organics. The binned wet PNSD is calculated using the parameters
 270 describing a dry log-normal PNSD (N_i , D_i , σ_i), information on aerosol chemical composition (mass fractions of
 271 chemical species), initial RH and temperature – all given as inputs for the model. When co-condensation is turned
 272 on, PARSEC-UFO takes in the summed volatility distributions (gas+particle phase i.e., $C_{g+p,q} = C_{g,q} + C_{p,q}$) –
 273 corrected for the PARSEC-UFO initialization temperature offline (Sect. 2.3) – as input. It is then assumed upon
 274 PARSEC-UFO initialization that the gas and particle phase are in equilibrium under the initialization RH. Finally,
 275 PARSEC-UFO solves partitioning coefficients for each volatility bin (ξ_q) i.e., the distribution of organic mass
 276 between gas and particle phase:

$$\xi_q \equiv \frac{C_{p,q}}{C_{p,q} + C_{g,q}}, \quad (14)$$

277 where the total particle phase organic mass concentration across all volatility bins is

$$C_p = \sum_q C_{p,q} = \sum_q C_{g+p,q} \xi_q \quad (15)$$

278 and the partitioning coefficients depend on C^* as follows

$$\xi_q = \frac{C_p}{C_p + C_q}. \quad (16)$$

279 Each ξ_q is solved iteratively from Equations (15–16) following absorptive partitioning theory including water
 280 (Barley et al., 2009), as it was done by Topping et al. (2013) assuming equilibrium conditions. The iterative
 281 method is possible, as C_p is constrained by the initial PNSD and the organic mass fraction, and the relative
 282 proportions of the volatility bins (volatility distribution shape) are preserved. As assuming equilibrium conditions

283 limits the amount of organic vapor available for co-condensation, it may also reduce the cloud response to co-
284 condensation. Therefore, the initial organic vapor concentrations provided here can be taken as a lower limit.

285 Overall, 97 daytime scenarios (local time between 10:00 and 19:00) are simulated adiabatically with
286 PARSEC-UFO. The initialization data originate from the Biogenic Aerosols – Effects on Clouds and Climate
287 (BAECC) campaign, which took place in 2014 at the Station Measuring Ecosystem–Atmosphere Relationships
288 (SMEAR) II in Hyytiälä, Finland (Petäjä et al., 2016). The measurements and data processing relevant to this
289 study are described in Sect. 2.3. The configuration of PARSEC-UFO used in this study only considers the
290 adiabatic ascent of an air parcel, without treatment of variable vertical updraft during ascent, droplet collision and
291 coalescence or entrainment. The simulations are performed for fixed updraft velocities of 0.1 m s^{-1} , 0.3 m s^{-1} , and
292 1.0 m s^{-1} , with and without co-condensation. During the CPM simulation period, SMEAR II was under daytime
293 clouds roughly 50–60% of the time (Ylivinkka et al., 2020), which were most often low level clouds motivating
294 selection of updraft velocities. The initial atmospheric pressure and relative humidity are set to 980 hPa and 90%,
295 respectively, in all simulation scenarios, unless otherwise stated. The PARSEC-UFO initialization temperature
296 varies throughout the simulation set, and is taken from interpolated radiosonde data that represents the 90%
297 initialization RH (Sect. 2.3). The selection of the 90% RH was motivated by the previous study by Crooks et al.
298 (2018). However, we acknowledge that more work is needed to better harmonize this parameter, along with
299 initialization pressure, to in-situ aerosol measurements. Each modelled scenario has log-normal parameters
300 describing a bimodal aerosol size distribution from BAECC measurements and the organic mass fraction from
301 ACSM measurements (Sect. 2.3). The rest of the mass is assumed to be ammonium sulfate, although an ion pairing
302 method (Äijälä et al., 2017) would suggest significant contributions also from ammonium bisulfate (For
303 the simulations performed here, BC is not included given its small (about <5%) contribution to aerosol mass from
304 late spring to summer (Luoma, 2021). While PARSEC-UFO does not utilize κ -Köhler theory (Petters and
305 Kreidenweis, 2008), it might be useful to know that the assumed hygroscopicity, if translated to the hygroscopicity
306 parameter κ , would be 0.14 and 0.72 for organics and ammonium sulfate, respectively (ideal solution; median κ_{tot}
307 ≈ 0.32). The assumed overall hygroscopicity is therefore likely to be overestimated, and it would exceed κ
308 determined for SMEAR II experimentally in previous studies (e.g., Sihto et al., 2011 suggest $\kappa = 0.18$). Due to
309 the likely overestimation of aerosol liquid water at initial conditions, it is also likely that the amount of organic
310 vapor available for co-condensation after PARSEC-UFO initialization is underestimated.

311 Table 1 contains a summary of the simulation input data along with the values used for mass
312 accommodation coefficient, surface tension, the vaporization enthalpy and effective soluble fraction of organics
313 as well as the number of PNSD size bins. A more comprehensive look into the input data can be found in Table
314 S.1. The simulation output at 50 m above cloud base, discussed later in the results section of the paper (Sect. 3),
315 is summarized in Table 2. Particles exceeding the critical radius (calculated by Köhler theory) in their wet radii
316 are considered as cloud droplets in this work. The output data are averaged to a fixed height output grid spaced
317 with a two-meter resolution until 200 meters above cloud base.

318 **2.3 PARSEC-UFO input data measurements and processing**

319 The observational data used as PARSEC-UFO input (Fig. 1) were collected during the BAECC campaign which
320 took place in 2014 at SMEAR II station in Hyytiälä, Finland (Petäjä et al., 2016). SMEAR II is a well characterized
321 atmospheric measurement supersite located within a boreal forest in Southern Finland ($61^{\circ}51'N$, $24^{\circ}17'E$; Hari
322 and Kulmala, 2005). The surroundings of the measurement site are mostly forested (80% within a 5 km radius

323 and 65% within a 50 km radius; Williams et al., 2011). The atmospheric composition measured at the site suggests
324 strong influence of biogenic emissions on aerosol and aerosol precursor (i.e., biogenic VOCs, BVOCs)
325 concentrations (e.g., Hakola et al., 2012; Yan et al., 2016; Allan et al., 2006; Heikkinen et al., 2021).
326 Anthropogenic influence is pronounced when air masses arrive from heavily industrialized areas such as St
327 Petersburg, Russia (Kulmala et al., 2000).

328 As PARSEC-UFO simulations are initialized at 90% RH, which is most of the time higher than that
329 measured at ground level, an interpolated radiosonde data product from the BAECC campaign (ARM Data Center,
330 2014) is used to find temperatures matching 90% RH. Radio soundings are performed four times a day (Petäjä et
331 al., 2016). Both the temperature measured near ground level (8.4 m above ground level) and the temperature
332 corresponding to 90% RH are shown in Fig. 1c. While these temperatures show similar temporal behavior at
333 times, also major differences exist, arising e.g., from instable temperature profiles as well as sudden changes in
334 air masses that the interpolated data product built from sondes sent three times a day fails to capture. A well-
335 mixed boundary layer is assumed, and therefore the dry PNSD and aerosol chemical composition are assumed
336 suitable as such for PARSEC-UFO input.

337 The PNSD for the PARSEC-UFO initialization are obtained from the Differential Mobility Particle Sizer
338 (DMPS) measurements from SMEAR II performed within the forest canopy (Aalto et al., 2001; Petäjä et al., 2016;
339 Fig. 1a). Since PARSEC-UFO takes in the log-normal parameters that the size distribution comprises (N_i , D_i , σ_i)
340 also the fitting of the PNSD is performed. This is done using the Hussein et al. (2005) algorithm that allows fitting
341 1–4 modes into the measured distributions and decides the optimal number of modes. For the BAECC data set,
342 the optimal number would always be between three and four modes, with a higher number of modes generally
343 yielding a better fit to the observational data as expected. Despite the optimal number of 3–4 modes, the maximum
344 number of modes is restricted to two as the agreement between the fitted and measured distributions remained
345 good considering the experimental uncertainties (Fig. S.1). Statistics regarding the log-normal parameters of the
346 fitted data during BAECC are provided in Tables 1 and S.1. The bimodal PNSD fits are also calculated for the
347 years 2012–2017. These data are used later to evaluate the frequency of times size distributions yielding high
348 Δ CDNC appear in long-term in-situ data.

349 The aerosol chemical composition for PARSEC-UFO initialization are obtained from Aerosol Chemical
350 Speciation Monitor (ACSM; Ng et al., 2011) measurements performed within the forest canopy (Heikkinen et al.,
351 2020). The ACSM measures the non-refractory (NR) sub-micrometer particular matter (PM_{10}) chemical
352 composition, which means that the reported composition is restricted to organics, sulfate, nitrate, chloride and
353 ammonium. The salts measured by the instrument do not include sea salt, because it typically exists in the coarse
354 mode and does not fully evaporate at the ACSM vaporizer temperature of 600°C. The latter reason restricts the
355 instrument also from detecting black carbon (BC). The composition from the ACSM measurements is shown in
356 Fig. 1b. Statistics regarding the organic mass fractions (f_{org}) are shown in Table 2. The ACSM data are further
357 used to derive volatility distributions similar to those utilized by Topping et al. (2013; see Sect. 2.3.1 for details).
358 The volatility distributions derived from ACSM are termed as CJ in the following. The letter combination refers
359 to Cappa and Jimenez (2010), the source of the volatility distribution shapes determined for different OA types.
360 The construction of CJ distributions suitable as PARSEC-UFO input data is explained in Sect. 2.3.1.

361 The Filter Inlet for Gases and AEROSols (FIGAERO; Lopez-Hilfiker et al., 2014) coupled with a
362 chemical ionization mass spectrometer (CIMS; the coupling of these instruments hereafter referred to as

363 FIGAERO-I-CIMS), sampling above the forest canopy in a ca. 30 m tower, is used to retrieve molecular
364 composition and volatility distributions of gas- and particle-phase species during BAECC (Mohr et al., 2017,
365 2019; Schobesberger et al., 2016; Lee et al., 2018, 2020; see Sect. 2.3.2 for details). The FIGAERO-I-CIMS
366 stands as one of the very few instruments capable of performing near-simultaneous measurements of both gas and
367 particle phases. The FIGAERO inlet allows the gas phase to be sampled while aerosol particles are collected on a
368 Teflon filter, and after sufficient particle deposition time the sample is heated and the evaporated molecules are
369 measured similarly to the gas phase. The heating procedure, which typically reaches a maximum temperature of
370 around 200°C can, however, cause thermal fragmentation of molecules (Lopez-Hilfiker et al., 2015). This leads
371 to the detection of small molecular fragments, which get assigned a higher C^* than that of the parent molecule,
372 which can be seen in the FIGAERO-I-CIMS thermograms when compounds with high C^* vaporize at
373 exceptionally high temperatures. In addition to the indistinguishable isomers from any of the phases from online
374 FIGAERO-I-CIMS measurements (or any other mass spectrometer for that matter), thermal fragmentations add
375 to the uncertainty of volatility distributions retrieved from these data. The derivation of the volatility distributions
376 derived from FIGAERO-I-CIMS data (termed F distributions in the following) is explained in Sect. 2.3.2.

377

378 2.3.1 Volatility distributions from ACSM data (CJ distributions)

379 Previous to the development of the FIGAERO-I-CIMS, organic volatility distributions were probed only through
380 particle phase measurements (e.g., Huffman et al., 2009b), which enabled volatility constraints of relatively low
381 volatility species (Cappa and Jimenez, 2010). More precisely, these early generation OA volatility distributions
382 were obtained from e.g. Aerosol Mass Spectrometer (AMS; Canagaratna et al., 2007) measurements coupled with
383 a thermal denuder (TD; e.g., Huffman et al., 2009a, b). The TD-AMS measurements provide thermograms (mass
384 fractions remaining in the particle phase as a function of TD temperature of ca. 25–250 °C) that could be assigned
385 to individual OA components i.e., low-volatility oxygenated organic aerosol (LV-OOA), semi-volatile
386 oxygenated organic aerosol (SV-OOA), hydrocarbon-like OA (HOA) and biomass burning OA (BBOA). Cappa
387 and Jimenez (2010) then reproduced such thermograms using a kinetic evaporation model (Cappa, 2010) through
388 fitted OA volatility distributions. In this paper, volatility distributions of this kind are referred to as CJ
389 distributions.

390 To calculate the CJ distributions for the BAECC OA types, the LV-OOA, SV-OOA and primary organic
391 aerosol (POA; taken as a mix of HOA and BBOA) from the SMEAR II ACSM long-term data set are utilized
392 (Heikkinen et al., 2021). During BAECC, the organic aerosol comprised 63% LV-OOA, 32% SV-OOA and only
393 5% POA on average. Using the time-dependent mass fractions of each OA type, mass-weighted average CJ
394 volatility distributions for each of the model initialization scenarios (97 of them) are calculated. The CJ
395 distribution shapes are taken from Cappa and Jimenez (2010), and they are provided under 298.15 K.

396 As the CJ volatility distributions have been reported for 298.15 K (Cappa and Jimenez, 2010), and
397 PARSEC-UFO simulations are generally initialized at lower temperatures (Fig. 1c), accounting for the impact the
398 temperature reduction has on C^* is necessary. The relationship between temperature and C^* is accounted for using
399 the Arrhenius-type Clausius-Clapeyron relation (Eq. 13), where T is the ambient temperature in Kelvin (the
400 PARSEC-UFO initialization temperature), and T_{ref} is 298.15 K. For the relationship between ΔH_{vap} and $C^*(T_{\text{ref}})$,
401 the formulation provided in Epstein et al. (2010) is used:

$$\Delta H_{\text{vap}} = -11 \log_{10} C^*(T_{\text{ref}}) + 129, \quad (17)$$

402 where ΔH_{vap} is the change in heat (enthalpy) of vaporization in kJ mol^{-1} . A lower limit of 20 kJ mol^{-1} is set to the
 403 ΔH_{vap} , which is close to the ΔH_{vap} determined for formic acid (NIST Chemistry WebBook, 2022). Eq. (17) would
 404 otherwise provide too low, unphysical and even negative values. The temperature adjustment (Eq. 13), does not
 405 change the shape of the volatility distribution, but the volatility distribution x -axis shifts to the left. See example
 406 in Fig. S.2. After the temperature adjustments, the volatility distributions are binned to ranges between $\log_{10} C^* =$
 407 $[-8, 3]$ spaced by one decade in C^* . The lower limit is reduced by two orders of magnitude ($C^*(T_{\text{ref}}) = [-6, 3]$), but
 408 the upper limit remains as the initialization temperatures did not exceed T_{ref} . The campaign average CJ volatility
 409 distribution is shown with black bars in Fig. 2a. However, each simulation utilizes a unique distribution
 410 constructed using the LV-OOA, SV-OOA, and POA time series.

411

412 2.3.2 Volatility distributions from FIGAERO-I-CIMS data (F distributions)

413 Organic aerosol volatility distributions from FIGAERO-I-CIMS measurements conducted during BAEEC (Mohr
 414 et al., 2017, 2019; Schobesberger et al., 2016; Lee et al., 2018, 2020) are also derived. It can be assumed that the
 415 FIGAERO-I-CIMS detected most of the OA measured with the ACSM, because FIGAERO-I-CIMS is sensitive
 416 to oxidized organic species, such as organic acids (Lutz et al., 2019), and most of the observed OA mass (~95%)
 417 measured by the ACSM can be attributed to oxygenated organic aerosol – thought to represent organic acids
 418 (Yatavelli et al., 2015). The agreement between the two measurements is supported by the comparison between
 419 the daytime FIGAERO-I-CIMS particle phase signal (of identified ions) and the OA mass concentration retrieved
 420 from ACSM measurements provided in Fig. S.3. While the quantification of the FIGAERO-I-CIMS
 421 measurements remains challenging and therefore whilst a quantitative comparison between the concentrations is
 422 uncertain, the high correlation between measurement data (Pearson $R = 0.79$) proves that the instruments generally
 423 sample the same aerosol population. Notably, the PARSEC-UFO simulations use OA mass fraction (f_{Org}) only
 424 from the ACSM measurements. The volatility distributions are derived from FIGAERO-I-CIMS data using
 425 molecular formula parameterizations derived under 300 K in Li et al. (2016):

$$\log_{10} C^*(T_{\text{ref}}) = (n_C^0 - n_C) b_C - n_O b_O - 2 \frac{n_C n_O}{(n_C + n_O)} b_{\text{CO}} - n_N b_N, \quad (18)$$

426

427 where n_C^0 is a reference carbon number; b_C , b_O , and b_N are the contributions of each carbon, oxygen, and nitrogen
 428 atom to the $\log_{10} C^*$, respectively; b_{CO} is a so-called carbon-oxygen non-ideality parameter (Donahue et al., 2011);
 429 n_C , n_O , and n_N are the numbers of carbon, oxygen, and nitrogen atoms in the molecular formulae assigned for the
 430 FIGAERO-I-CIMS data during high resolution peak fitting of the measured mass spectra. The b -values utilized
 431 are listed in Li et al. (2016). In their recent work, Huang et al. (2021) derived volatility distributions from various
 432 organic vapor measurements from SMEAR II. They adjusted the Li et al. (2016) parameterization for organic
 433 nitrates. As shown in Isaacman–VanWertz and Aumont (2021), the utilization of the Li et al. (2016)
 434 parameterization for OA rich in organic nitrates leads to biased vapor pressure estimates. Organic nitrates are
 435 known to form in the boreal air as a result of nitrate radical chemistry, which is pronounced during night, along
 436 with daytime oxidation of monoterpenes in the presence of nitric oxide (e.g., Yan et al., 2016; Zhang et al., 2020).
 437 To account for these nitrates, Huang et al. (2021) followed the suggestions presented in Daumit et al. (2013) and
 438 treated all the nitrate functional groups as hydroxyl ($-\text{OH}$) groups. Given that the focus of this study is on the

439 same measurement site as Huang et al. (2021), their methodology for deriving a volatility distribution from the
440 FIGAERO-I-CIMS is followed here. Once the volatility distributions are constructed using Eq. (18) for 300 K
441 (reference temperature), their adjustments to the parcel model simulation initial temperatures using Eq. (13) is
442 performed.

443 The volatilities are calculated for the 1596 ions identified by the FIGAERO-I-CIMS measurements.
444 Afterwards the signals are binned with a decadal spacing so that all the ELVOC and LVOC are summed into one
445 bin at $C^* = 10^{-4} \mu\text{g m}^{-3}$. The highest volatilities reached $C^* = 10^7 \mu\text{g m}^{-3}$, which is therefore set as the upper limit
446 of the volatility distribution. Following from this, the volatility span is $\log_{10}C^* = [-4, 7]$. The campaign average
447 volatility distribution is shown in red bars in Fig. 2a. The average CJ distribution exhibits generally higher
448 fractions in the ELVOC region as compared to the F distribution (Fig. 2a). This mostly results from the low/non-
449 existent SVOC and IVOC concentrations in the CJ distribution. As the ELVOCs and LVOCs contain little or no
450 gas phase signals post-initialization, the F distribution used as input for PARSEC-UFO simulations uses the
451 volatility span of $\log_{10}C^* = [0, 7]$ to speed up the simulations.

452 The average F distribution shows a remarkable agreement with the organic volatility distributions from
453 the BEACHON-RoMBAS field campaign conducted at the Manitou Experimental Forest Observatory in the
454 Colorado Rocky Mountains in summer 2011 (Hunter et al., 2017, see Fig. 2a). Initially, Hunter et al. (2017)
455 derived a volatility distribution for the total atmospheric reactive carbon (other than CH_4 , CO_2 and CO) using six
456 different types of measurements and assuming minimal overlap among the measured species. Here, the Hunter et
457 al. (2017) distribution is displayed in Fig. 2a after shifting it to the mean PARSEC-UFO initialization temperature
458 (280 K) using Eq. (13) and subtracting non-oxygenated VOC signals from it for comparison. The Hunter et al.
459 (2017) distribution is not used in PARSEC-UFO simulations, it is only shown for comparative purposes due to its
460 similarity with the F distributions.

461 In Figs. 2b and c, the partitioning coefficients ξ_g from the PARSEC-UFO initialization (see Sect. 2.2) are
462 compared against the partitioning suggested by the FIGAERO-I-CIMS measurements, where the C^* represent the
463 mean PARSEC-UFO initialization temperature and range from $\log_{10}C^* = [-4, 7]$. The concentrations in volatility
464 bins with $\log_{10}C^* \leq 1$ agree, suggesting that the majority of the organics in these bins are in the particle phase.
465 Similarly, the agreement in the highest volatility bin ($\log_{10}C^* = 7$) suggests the presence of gas-phase compounds
466 only in both distributions. The estimations of the gas phase vary between $\log_{10}C^* = [1, 7]$, showing a higher gas-
467 phase fraction for the modelled partitioning coefficients (Fig. 2b–d). This variability can result from numerous
468 reasons, which apart from uncertainties related to measurements and parametrizations include viscous particle
469 coatings inhibiting equilibration between gas and particle phases, and therefore showing high particle-phase
470 concentrations of high-volatility compounds in the observations. Alternatively, these concentrations can also
471 result from thermal decomposition of lower volatility products during the FIGAERO-I-CIMS heating process
472 (Lopez-Hilfiker et al., 2015) or from the tendency of the Eq. (18) parameterization to underestimate the volatility
473 of organic nitrates (Graham et al., 2022; despite treating the $-\text{NO}_3$ groups at $-\text{OH}$ groups), shown to be abundant
474 in the BAECC FIGAERO-I-CIMS data set (Fig. 2e). Understanding these differences is important and requires
475 further analysis.

476 The molecular composition of the gas-phase compounds detected by the I-CIMS during BAECC are
477 analyzed and presented in detail in Lee et al. (2018). In the following, the average composition of each volatility
478 bin during daytime is briefly described. Except for the highest volatility bin, nitrogen-containing species (CHON),

479 which are prominently organic nitrates at SMEAR II (Huang et al., 2021), make up significant mass fractions of
480 each bin in the gas phase (Fig. 2e). Fig. 2f shows the concentration of the gas-phase compounds as a function of
481 the compound carbon and oxygen atom numbers. The figure shows how ELVOCs and LVOCs have the highest
482 numbers of both carbon and oxygen atoms. IVOCs and SVOCs comprise compounds with highly variable carbon
483 skeleton lengths, but the number of oxygen atoms per compound remains low, notably always lowest for IVOCs
484 and VOCs. Formic acid (HCOOH) makes up most of the gas phase signal. It is distributed in the most volatile
485 volatility bin ($C^* = 10^7 \mu\text{g m}^{-3}$). HCOOH is one of the most abundant carboxylic acids in the atmosphere and rain
486 water (e.g., Galloway et al., 1982; Millet et al., 2015 and references therein) and is known to have various sources
487 and precursors (Millet et al., 2015). The I-CIMS measurements discussed here were also performed as part of an
488 eddy covariance flux measurement setup during BAEC (Schobesberger et al., 2016). These flux measurements
489 provided insight into the high HCOOH concentrations possibly due to high emissions from the boreal forest
490 ecosystem. More details from these results can be found in Schobesberger et al. (2016).

491

492 **2.4 UK Earth System Model (UKESM1) simulations**

493 To evaluate the frequency of times size distributions yielding high ΔCDNC (which is the percent-change in CDNC
494 due to co-condensation) during BAEC would become evident over the boreal biome in an ESM if a
495 parameterization of co-condensation was implemented, the United Kingdom Earth System Model (UKESM1,
496 Sellar et al., 2019; Mulcahy et al., 2020) is utilized. The simulations performed with UKESM1 are configured for
497 Atmospheric Model Intercomparison Project (AMIP) style simulations, where UKESM1 is run in its atmosphere-
498 only configuration with time-evolving sea surface temperature and sea ice as well as prescribed marine biogenic
499 emissions from fully coupled model simulations. In addition to the HadGEM3-GC3.1 core physical dynamical
500 model of the atmosphere, land, ocean and sea ice systems (Ridley et al., 2018; Storkey et al., 2018; Walters et al.,
501 2017), UKESM1 also contains additional component models for atmospheric chemistry and ocean and terrestrial
502 biogeochemistry for carbon and nitrogen cycle representation. The version of UKESM1 used includes
503 developments to the droplet activation scheme from Mulcahy et al. (2020) to facilitate more consistent
504 comparisons against PARSEC-UFO. In the standard configuration of UKESM1, aerosol particles are activated
505 into cloud droplets using the droplet activation parameterization of Abdul-Razzak and Ghan (2000). An alternative
506 optional configuration of UKESM1 was employed that uses the Barahona et al. (2010) droplet activation
507 parameterization, which has been shown to be more consistent when compared against an adiabatic cloud parcel
508 model over a range of conditions (Simpson et al., 2014; Partridge et al., 2015). Furthermore, in the standard
509 configuration of UKESM1, the droplet activation scheme uses the distribution of sub-grid variability of updraft
510 velocities according to West et al. (2014) with updates as described in Mulcahy et al. (2018). To facilitate more
511 consistent comparisons against PARSEC-UFO simulations that calculate droplet number using a single average
512 updraft velocity, the single characteristic updraft velocity (Peng et al., 2005) was used to initialize the droplet
513 activation scheme in UKESM1.

514 A N96L85 horizontal resolution structure ($1.875^\circ \times 1.25^\circ$ longitude–latitude, which corresponds roughly
515 a horizontal resolution of 135 km) is chosen for the simulations and the vertical space is split to 85 levels (50
516 levels between 0 and 18 km and 35 levels between 18 and 85 km). In this study the model is run in a nudged
517 configuration (horizontal wind nudging (but not temperature) between model levels 12 and 80 with a constant 6-
518 hour relaxation time), for the years 2009–2013 inclusively. External forcing and emission datasets are consistent

519 with the Coupled Model Intercomparison Project Phase 6 (CMIP6) implementation as described in Sellar et al.
520 (2020). The simulation setup is same as in the Aerosol Comparisons between Observations and Models
521 (AeroCom) Phase III GCM Trajectory experiment (AeroCom, 2022; Kim et al., 2020).

522 The UKESM1 aerosol scheme represents the particle size distributions with five log-normal modes: the
523 nucleation soluble mode, Aitken soluble and insoluble modes, accumulation soluble mode, and coarse soluble
524 mode (Mulcahy et al., 2020). The aerosol microphysical processes of new particle formation (NPF), condensation,
525 coagulation, wet scavenging, dry deposition and cloud processing are handled with GLOMAP (Global Model of
526 Aerosol Processes; Mann et al., 2010; Mulcahy et al., 2020). The UKESM1 NPF mechanism follows the
527 parameterization derived in Vehkamäki et al. (2002) for binary homogeneous nucleation of H₂SO₄ and water.
528 Separate boundary layer NPF is not included in the simulations (Mulcahy et al., 2020). The soluble aerosol size
529 distribution lognormal aerosol modal parameters (nucleation mode, soluble Aitken mode and soluble
530 accumulation mode) and sub-grid scale updraft velocities with a 3-hour time resolution at cloud base of stratiform
531 clouds are used. These diagnostics are subsequently masked to include only data in which activated aerosol
532 particles exceeds zero and the temperature exceeds 237.15 K in keeping with criteria used by the droplet activation
533 scheme. The PNSD modal parameters are used to construct aerosol size distributions. In UKESM1 the geometric
534 standard deviations are fixed parameters. The same values are used for consistency for the modes that are
535 accounted for in this work. The geometric standard deviation for UKESM1 Nucleation soluble mode and the
536 Aitken soluble mode is 1.59, and for the accumulation soluble mode it is 1.40. UKESM1 outputs for the Aitken
537 insoluble mode and coarse mode are not used in analysis performed in this study because they do not contribute
538 to CCN in the model representation of cloud droplet activation. UKESM1 uses a 26% SOA yield from
539 monoterpenes, the emissions of which are from The Model of Emissions of Gases and Aerosols from Nature
540 (MEGAN) version 2.1 (Guenther et al., 1995).

541 **3 Results and discussion**

542 **3.1 Organic condensation: time and volatility dependencies**

543 The first PARSEC-UFO simulation results (Fig. 3) correspond to initializing the model with data collected on
544 May 11, 2014 at 13:37 EET (East European winter time). This simulation is identified from the full dataset as one
545 that represents a median cloud response to co-condensation of organics and water. Figure 3a shows the vertical
546 evolution of total SVOC and IVOC concentrations in the gas phase for the three different updraft scenarios ($w =$
547 0.1, 0.3, or 1 m s⁻¹, respectively). Both SVOC and IVOC concentrations decrease significantly along the adiabatic
548 ascent in subsaturated conditions below cloud base (CB). Given that the PARSEC-UFO simulation output is saved
549 with 2-meter vertical resolution, “below CB” contains all the simulation output under subsaturated conditions,
550 and the RH at CB is defined as $\min(\text{RH} \geq 100 \%)$. When moving to saturated conditions, SVOCs and IVOCs are
551 scavenged. This result is in line with Bardakov et al. (2020), who modelled complete gas removal of volatility
552 bins up to roughly $\log_{10}C^* = 9$ within convective clouds.

553 When considering all 97 simulations, the net mass fractions of organics condensed below CB are on
554 average 91, 70 and 28% for the 0.1, 0.3 and 1.0 m s⁻¹ updraft, respectively, which in absolute concentrations means
555 additions of 1.8, 1.4, and 0.7 $\mu\text{g m}^{-3}$ to the aerosol particle soluble mass (Table 2). The yielded mass concentrations
556 are in the same order of magnitude as the PM₁ mass concentrations measured during BAEC (interquartile range,
557 IQR: 0.95, 1.95, and 3.22 $\mu\text{g m}^{-3}$ from ACSM data), which means that such organic condensation along the

558 adiabatic ascents as simulated here would yield roughly a doubling of the soluble mass due to SVOC and IVOC
559 condensation below CB. Figures 4d–f show the simulated organic condensate concentrations for each volatility
560 bin. While the condensed fraction for the highest volatility bin is smallest (Figs. 4a–c), the absolute concentrations
561 of condensate are amongst the largest due to the high availability of organic vapor in the highest volatility bin
562 (mostly HCOOH; Sect. 2.3.2). The condensation efficiency of the highest volatility bin correlates with the number
563 of large particles serving as condensation sink for vapors (Fig. S.4). This suggests that these organic vapors are
564 likely to condense onto larger particles, which are susceptible to be activated into cloud droplets regardless of co-
565 condensation. Similar correlations are observed to a lesser extent with the $\log_{10}C^* = 6$ volatility bin (not shown).
566 In this work, the information of the size ranges of particles which the high-volatility IVOCs condense onto is
567 lacking. Therefore, more systematic studies should be conducted to better understand whether the condensation
568 of the high-volatility IVOCs onto ultrafine particles is sufficient enough to lead to increased droplet activation.

569 The exact numbers presented here should, however, be assessed with caution as an ideal liquid phase, as
570 well as partitioning being determined by mole fractions of water-soluble organics are assumed (Sect. 2.1.1).
571 Topping et al. (2013) looked into the assumption of ideality in their supplementary material. They found it to
572 enhance the amount of modelled organic condensate as compared to a non-ideal case. However, their simulations
573 exploring non-ideality with organic activity coefficients predicted with the UNIFAC method (UNIQUAC
574 Functional-group Activity Coefficients; Fredenslund et al., 1975) still led to significant amounts of condensed
575 organic mass. The impact of the ideality assumption was shown to be most significant in their highest volatility
576 bin ($C^* = 1000 \mu\text{g m}^{-3}$). Activity coefficients (and solubilities) of organics should in the future be better constrained
577 to assess the impact on volatility bins of $\log_{10}C^* > 3$, which was not explored in Topping et al. (2013). As discussed
578 in the Topping et al. (2013) supplementary information, it is likely that solubility decreases towards the higher
579 volatility bins. Here, a simple assessment of the assumption of ideality (Appendix A, Fig. A.2b) suggests that the
580 gained organic soluble mass reduces only when the overall mass accommodation coefficient for organics is less
581 than 0.4. This would mean that the organic condensation shown here could be taken as the upper limit.

582 Further investigation on how efficiently different volatility bins condensed along the adiabatic ascents
583 across all the 97 simulation scenarios repeated with the three fixed updraft velocities is also performed (Fig. 4a–
584 c). In the 0.1 m s^{-1} updraft scenario, almost all organic vapor condenses up to $\log_{10}C^* = 5$ and the condensation
585 capability of the highest volatility bin ($\log_{10}C^* = 7$) shows the highest variability (~20–91% condensed below CB;
586 Fig. 4a). The same features can be observed with the 0.3 m s^{-1} and 1.0 m s^{-1} updraft simulations, although the
587 fraction of organic vapor condensed per volatility bin is reduced (in the $w = 1 \text{ m s}^{-1}$ scenarios only ca. 30% of the
588 vapor condenses below CB (Figs. 4b–c). The results from these simulations reveal that there is enough time only
589 under slow adiabatic ascents for most of the organic vapor to condense.

590

591 **3.2 Impact of meteorological conditions on the sensitivity of cloud microphysics to organic vapor** 592 **condensation**

593 As explained previously in Topping et al. (2013), the CDNC enhancements associated with co-condensation arise
594 from the increase in organic solute concentration, which decreases the critical supersaturation (s^*) needed for a
595 given particle to activate. The s^* is reduced about 10–20% for the May 11, 2014 at 13:37 EET case presented in
596 Fig. 3b when co-condensation is enabled. This reduction is calculated for a particle with a dry radius of 71.9 nm
597 (i.e., the smallest activated dry radius when co-condensation is disabled, r_{noCC}^*). Fig. S.5 shows the development

598 of the wet particle size as a function of altitude in the PARSEC-UFO simulation summarized in Fig. 3. It clearly
 599 demonstrates the differences introduced by co-condensation through the activation of new size bins (4 size bins
 600 in total when $w = 0.1 \text{ m s}^{-1}$) that would have remained as interstitial aerosol particles in the simulations where co-
 601 condensation is turned off. The enhanced growth of more particles due to co-condensation enhances the water
 602 vapor condensation sink, which leads to a reduction in the achieved maximum ambient supersaturations (s_{max} ; see
 603 Fig. 3c for the May 11 case and Table 2 summarizing all the 97 simulations). As the meteorological conditions
 604 are the same in simulations performed with and without co-condensation, the condensation sink dictates the
 605 changes in s_{max} (Eq. 3). A reduced s_{max} would typically lower the number of aerosol particles activating into cloud
 606 droplets, but here the reductions in s^* are greater than the reductions in s_{max} , which therefore leads to an enhanced
 607 CDNC (see Fig. 3b–c for the May 11 case). This can be interpreted as a competition effect between the s_{max} and
 608 s^* reductions, respectively, which the s^* reduction wins. When examining the 0.1 m s^{-1} updraft case in the May
 609 11th simulation shown in Fig. 3, the s_{max} is reduced $\sim 7\%$, which is less significant than the s^* reduction of $\sim 20\%$.
 610 This leads to a 22% enhancement in CDNC (Fig. 3d) as r^* reduces from 72 nm to 66 nm ($\Delta r^* \approx 6 \text{ nm}$). Fig. 3e
 611 shows the droplet spectrum for the May 11 case, which highlights the consistent shift of droplet sizes to smaller
 612 diameters due to organic co-condensation (see also Fig. S.5, which displays the same May 11th simulation with w
 613 $= 0.1 \text{ m s}^{-1}$). The impact such shift could have on cloud lifetime and precipitation should be studied further.

614 The modelled BAECC campaign median CDNC values (over the 97 simulations) without co-
 615 condensation are on average 161, 300 and 530 cm^{-3} in modeling scenarios utilizing 0.1 m s^{-1} , 0.3 m s^{-1} , and 1.0 m s^{-1}
 616 updrafts, respectively (Table 2). CDNC is shown to correlate well with the accumulation mode number
 617 concentration (N_2), and at times with the Aitken mode number concentration (N_1) if the Aitken mode particles are
 618 large enough in size and accompanied with strong enough updrafts and a low N_2 (Fig. S.6). The reductions in the
 619 smallest activated dry radii due to co-condensation ($r_{\text{noCC}}^* - r_{\text{CC}}^*$) are on average ~ 8 , ~ 7 , and $\sim 5 \text{ nm}$ for the modeling
 620 scenarios utilizing 0.1 m s^{-1} , 0.3 m s^{-1} , and 1.0 m s^{-1} updrafts, respectively, and the corresponding median ΔCDNC
 621 are ~ 16 , ~ 23 and $\sim 19\%$, respectively (Table 2 and Fig. 5a). The swarm plot on Fig. 5a shows that ΔCDNC and
 622 CDNC do not correlate i.e., low CDNC in the noCC runs does not favor high ΔCDNC .

623 On average during the BAECC simulation period (97 simulations), the highest ΔCDNC are found when
 624 initializing the model with a 0.3 m s^{-1} updraft velocity (also visible in Fig. 3d for the May 11 case) followed by
 625 ΔCDNC predictions for the 1 m s^{-1} case. In the latter, high supersaturations are achieved leading to the formation
 626 of many cloud droplets, yet the effects of co-condensation remained less pronounced as the high ascent speed
 627 poses kinetic limitations for organic condensation (see Sect. 3.1 and Fig. 4). Despite the highest organic uptake in
 628 the 0.1 m s^{-1} updraft simulations (Fig. 4a, d), the ΔCDNC remains the lowest. This can be explained by the low
 629 s_{max} , which remains insufficient to activate small particles to cloud droplets ($r_{\text{noCC}}^* \sim 64 \text{ nm}$; Table 2). As the
 630 Aitken mode possesses most particles in terms of number (Table 1), the few nm reductions in r^* affect ΔCDNC
 631 the most when the r^* reduction takes place on the steep PNSD slopes (high $d/d\log_{10}D$ ($dN/d\log_{10}D$)) between the
 632 Aitken and accumulation mode. When the updraft velocity is low (0.1 m s^{-1}), the r^* are too large to overlap with
 633 the parts of the PNSD with a high slope even if r^* reduces greatly due to co-condensation. Due to the high updraft-
 634 dependency of the modelled ΔCDNC , future process modeling work should consider performing simulations
 635 following updraft probability density functions (PDF), as used in GCMs, and calculating PDF weighted CDNC
 636 (West et al., 2014). This way more weight will be given to lower updrafts, and the model outputs will be more
 637 robust since the air parcels do not experience single updrafts in reality.

638 Besides updraft velocity, the modeled Δ CDNC are also affected by PARSEC-UFO initialization
639 temperatures. This can be seen when the effect of the volatility distribution upgrade (from CJ to F) on the modelled
640 Δ CDNC is investigated. For this purpose, an additional set of PARSEC-UFO simulations using the CJ volatility
641 distribution are performed. The CDNC enhancements due to co-condensation attained with the CJ volatility
642 distribution are negligible (median Δ CDNC is 0; Fig. S.7) and therefore strikingly different from those presented
643 in Topping et al. (2013). The large difference in the modeled Δ CDNC between the F and CJ simulations arises
644 from the low amount of organic vapor available for condensation ($\sum C_g^{\text{INIT}}$ is only $0.10 \mu\text{g m}^{-3}$ in CJ simulations
645 while in the F simulations it is $2.05 \mu\text{g m}^{-3}$), which in turn results from the low PARSEC-UFO initialization
646 temperature attained from the radio soundings (Sect. 2.3). If the initialization temperatures were higher, more
647 organic vapor would remain in the gas phase after PARSEC-UFO initialization, and larger Δ CDNC could be
648 modeled. The simulations performed in Topping et al. (2013) were initialized at 298 K, which explains why they
649 report significant CDNC enhancements due to co-condensation using a similar CJ volatility distribution as used
650 here. We can reproduce the Topping et al. (2013) findings when increasing the initialization temperature with
651 PARSEC-UFO (see Fig. S.8) and also demonstrate that by decreasing the initialization temperature from 298 to
652 280 K (the BAEEC median temperature), the Δ CDNC modeled by Topping et al. (2013) should also be negligible
653 (Fig. S.8). These findings emphasize the critical role of the initialization temperature (and assumptions made on
654 equilibrium upon model initialization) that impacts the amount of organic vapor present in the gas phase prior to
655 the air parcel's ascent. Additionally, the result suggests high importance of organic vapors with saturation vapor
656 concentrations exceeding $\log_{10}C^* = 3$ (under 298 K) for co-condensation. If one were to utilize CJ distributions
657 in future co-condensation work, one could consider multiplying the highest volatility bins e.g., with a carefully
658 selected constant. Similar approaches have been used previously when modeling SOA formation from IVOCs (Lu
659 et al., 2018).

660 As the results from Fig. 4 underline the time-dependence of co-condensation (Sect. 3.1), it is worth
661 remembering that the PARSEC-UFO initialization RH is set to 90% where equilibrium conditions are assumed
662 (see Sects. 2.4 and 2.2). Therefore, the kinetic effects play a role only from 90% to 100% RH. Importantly, if the
663 initial RH was set to a lower value, more time would be available for co-condensation before reaching CB, and if
664 the initial RH was set to a higher value, less time would be available. On the other hand, due to the assumption of
665 initial equilibrium conditions, a lower initial RH also ensures a higher organic vapor concentration available for
666 co-condensation, and a higher initial RH reduces the organic vapor availability. Together with initial temperature,
667 the initial RH strongly control the amount of organic vapor available for co-condensation (Appendix A, Fig. A.1,
668 Fig. S.3) and thereby the amount of soluble organic mass yielded by the time the air parcel reaches cloud base.
669 While the decision of maintaining a fixed initial RH for the different simulations is proven useful for this study
670 as it eases the data interpretation process, it should be acknowledged that the initial RH could be better constrained
671 in future simulations. Naturally, the organic vapor condensation depends on the initial RH, and as a result Δ CDNC
672 is also sensitive to the selection of the initial RH (Fig. A.1). If the initial RH is set to 60%, CDNC enhancements
673 as high as $\sim 100\%$ could be expected, while if the initial RH is set to 99% the enhancements are expected to range
674 between 0 and $\sim 20\%$. This variation is greater than the impact the ideality assumption (or the selection of
675 vaporization enthalpy) has on Δ CDNC (Sect. 3.1, Appendix A).

676

677 3.3 Impact of initial aerosol size distribution and organic vapor concentration on the sensitivity of CDNC 678 to organic vapor condensation

679
680 As briefly mentioned in the previous section, PNSD affects Δ CDNC along with the initial meteorological
681 conditions. The importance of Aitken mode in Δ CDNC associated with turning co-condensation on in PARSEC-
682 UFO is exemplified in Fig. 5b for the 0.3 m s^{-1} updraft simulations. In this figure, the initial dry PNSD are averaged
683 from the simulations with the highest 25% and lowest 50% modelled Δ CDNC, respectively. The PNSD
684 corresponding to the highest 25% of the modelled Δ CDNC has a very minor accumulation mode and a large
685 Aitken mode (with respect to the mode total number concentrations i.e., N_2 and N_1 , respectively) with a diameter
686 (D_1) of $\sim 40 \text{ nm}$ (D_2 is $\sim 110 \text{ nm}$). It is named as PNSD_{NUM}, where NUM refers to a strong nascent ultrafine mode
687 characteristic of the shown size distribution. The PNSD_{NUM} gain the highest Δ CDNC despite a relatively small
688 change in the smallest activated dry radii, because of the steep PNSD slope in the size-range where the smallest
689 activated dry radii reduce (Fig. S.9). The slope compensates for a comparatively small reduction in the smallest
690 activated dry radii by sharply increasing the number of particles that activate, when co-condensation is enabled.
691 The PNSD corresponding to the lowest 50% of the modelled Δ CDNC is strongly bimodal, where the Aitken and
692 accumulation modes are almost equal in terms of N . Moreover, the two modes are separated by a clear Hoppel
693 minimum (Hoppel and Frick, 1990). Hoppel minimum is characteristic for aerosol populations, which have
694 undergone cloud processing. The PNSD associated with the lowest Δ CDNC tend to have the smallest activated
695 dry radii close to the Hoppel minimum, where the PNSD slope is negligible (Fig. S.10). Therefore, the integral
696 through this range provides less particles to be activated to cloud droplets, and the Δ CDNC remain low. It should
697 be noted, however, that the reductions in the smallest activated dry radii are on average higher in the simulations
698 initialized with PNSD_{NUM} (Fig. S.11a) due to higher availability of organic vapors (Fig. S.11b) and their
699 condensation to a more critical size range. Nonetheless, it is evident that the shape of the PNSD dictates the
700 magnitude of the Δ CDNC, as a $\sim 4 \text{ nm}$ reduction in the smallest activated dry radius can lead to a CDNC
701 enhancement of $\sim 45\%$ in the case of a PNSD_{NUM}, while in the case of a PNSD with a Hoppel minimum, Δ CDNC
702 would be only $\sim 10\%$ (Fig. S.11). These results underline that environments rich in particles from a local source
703 would be more susceptible to high Δ CDNC due to co-condensation while regions with aged and cloud processed
704 size distributions are affected less (here, Δ CDNC $<20\%$; Fig. 5a).

705 Interestingly, a PNSD_{NUM} was found to be important when looking into suitable conditions for large
706 increase in CDNC caused by surface active organics (Ovadnevaite et al., 2017; Lowe et al., 2019). Lowe et al.
707 (2019) utilized a similar CPM (ICPM, Sect. 2.1) as used in this study (notably without co-condensation), but
708 enabled a fraction of the particulate organics to form a thin, max. 0.2 nm thick film around the particle. The film
709 was characterized by a surface tension of 40 mN m^{-1} as opposed to the surface tension of pure water (72.8 mN m^{-1}).
710 The idea of this compressed film (CF) approach was to simulate the surface tension reductions caused by
711 organic species leading to the activation of smaller particles to cloud droplets at the coastal Mace Head site
712 (Ovadnevaite et al., 2017). Through sensitivity studies, Lowe et al. (2019) found that the largest percent change
713 in CDNC due to surface active organics ($>10\%$) took place in Mace Head when $N_2 < aN_1^b + c$ ($a = 602$, $b = 0.0884$,
714 $c = -766$). The increase in CDNC in the Lowe et al. (2019) study was also attributed to the reduction in s^* when
715 comparing against simulations where the surface tension was that of water. Moreover, the same competition effect
716 between s_{max} and s^* reductions – as described here in Sect. 3.2 – was demonstrated in their study, but just triggered
717 by different chemical parameters. The sensitivity of the CDNC enhancements to PNSD_{NUM} in this study as well

718 as in Lowe et al. (2019) demonstrates that the activation of fresh and non-cloud-processed aerosol particles is
719 susceptible to small reductions in s^* that can be triggered e.g., by organic surfactants or co-condensation.
720 Importantly, potential surface activity also affects the CCN activation behavior of atmospheric organics (Ruehl et
721 al., 2012, 2016; Lowe et al., 2019), correlating with volatility and solubility. The combined effect of all these three
722 properties needs to be thoroughly investigated in the future.

723 In conjunction with the ΔCDNC susceptibility to PNSD_{NUM} , this study most critically highlights the
724 importance of incorporating multimodal, and representative size distributions in process modeling studies
725 examining the cloud response to co-condensation (or surface-active organics as demonstrated in Lowe et al.,
726 2019). Topping et al. (2013), for example, used monomodal distributions (with varying log-normal parameters)
727 in their study, which could lead to overestimation of ΔCDNC as size distributions with Hoppel minima are not
728 explored. Multimodal distributions were used later by Crooks et al. (2018), but further explanation of the cloud
729 response of the update remained lacking. In summary, our results together with the Lowe et al. (2019) results
730 suggest that in clean environments with a local source of ultrafine particles, such as the boreal forest or marine
731 environments, organic species in the presence of a NUM-featured PNSD can have significant impact on cloud
732 properties either via co-condensation or through surface tension reductions.

733 Subsequently, a dry PNSD-based criteria for identifying regimes (conditions) in which co-condensation
734 has the highest impact on CDNC are defined. It is found that restricting the ratio between the accumulation and
735 Aitken mode geometric mean diameters in the initial dry PNSD to below six (i.e., $D_2/D_1 < 6$) and the Aitken mode
736 number concentration to exceed 1000 cm^{-3} (i.e., $N_1 > 1000 \text{ cm}^{-3}$) would yield $\Delta\text{CDNC} > 20\%$ in our simulations
737 (Fig. 5d). By using the diameter ratio criterion, size distributions without a distinguishable Hoppel minimum are
738 selected, which is characteristic in the simulations yielding the highest ΔCDNC (Fig. 5b) and the high N_1 ensures
739 a high concentration of aerosol particles potentially activating into cloud droplets.

740 In addition to the PNSD_{NUM} features, also the initial organic vapor concentration (C_g^{INIT}) influences the
741 modeled ΔCDNC . The extent to which the modeled ΔCDNC are sensitive to C_g^{INIT} is depicted in Fig. 5c using the
742 PARSEC-UFO simulations performed with 0.3 m s^{-1} updrafts. The y-axis represents the modeled ΔCDNC and
743 the x-axis the organic vapor concentration distributed in $\log_{10} C^*$ bins within $[-4, 4]$ (denoted as $C_{g, -4:4}^{\text{INIT}}$) i.e., in bins
744 that do not show high dependency on the available surface area (see Sect. 3.2 and Fig. S.4 for details). The
745 relationship is not straightforward, but linear increases in ΔCDNC as a function of $C_{g, -4:4}^{\text{INIT}}$ can be seen under
746 constant, yet sufficiently high s_{max} (here $> 0.2\%$). Under the modelled scenarios, where $s_{\text{max}} > 0.2\%$ the $C_{g, -4:4}^{\text{INIT}}$ is
747 generally low ($< 2 \mu\text{g m}^{-3}$). Still, the highest CDNC enhancements during the BAECC simulation period are
748 achieved under these conditions. The high CDNC enhancements can be achieved – despite the low organic vapor
749 abundance simply because the soluble organic mass is distributed to more smaller particles. The markers in Fig.
750 5c are color-coded by the initial PNSD surface area, which under a constant updraft anticorrelates with s_{max} (see
751 Eq. 3). ΔCDNC shows high sensitivity to $C_{g, -4:4}^{\text{INIT}}$ when the dry PNSD surface area stays below a $100 \mu\text{m}^2 \text{ cm}^{-3}$
752 threshold. Based on this analysis, it can be concluded that in the presence of a NUM-featured PNSD enabling the
753 formation of high supersaturations (the dry PNSD surface area stays below $100 \mu\text{m}^2 \text{ cm}^{-3}$), an adiabatic ascent
754 with an updraft of 0.1 or 0.3 m s^{-1} can yield ΔCDNC of $> 40\%$ if $1 \mu\text{g m}^{-3}$ of co-condensable organic vapor is
755 present in the rising air. This is a likely occurrence in the spring and summertime boreal forest (Huang et al.,
756 2021). However, it should be noted that under such scenarios the modeled ΔCDNC are highly sensitive to organic

757 vapor concentration (Fig. 5c) and a reduction of $\sim 0.5 \mu\text{g m}^{-3}$ in organic vapor concentration can half the modeled
758 CDNC when the PNSD surface area is low. The simulations performed with the highest updraft velocity ($w = 1.0$
759 m s^{-1}) yield lower ΔCDNC under these clean conditions (ΔCDNC does not exceed 40%) even though the simulated
760 s_{max} increase as opposed to the results obtained with lower updrafts (e.g., Table 2), because of the kinetic
761 limitations hindering co-condensation (see Sect. 3.1).

762

763 3.4 Expected seasonality in the impact of co-condensation on CDNC at SMEAR II

764 In the following, the seasonality of the dry PNSD surface area at SMEAR II (6-year-long time series, 2012–2017)
765 is investigated to estimate how often it stays below the previously mentioned threshold of $100 \mu\text{m}^2 \text{cm}^{-3}$ i.e., times
766 when only $1 \mu\text{g m}^{-3}$ of co-condensable organic vapor present in the rising air could yield significant ΔCDNC . This
767 is followed by an investigation of the frequency of the PNSD criteria ($D_2/D_1 < 6$ and $N_1 > 1000 \text{cm}^{-3}$) fulfillments in
768 the long-term size distribution measurements at SMEAR II.

769 Fig. 6a shows the seasonality of the dry surface area at SMEAR II. During daytime (9–19 EET) the
770 surface area stays below the previously mentioned threshold 86% of the time during the 2012–2017 measurement
771 period (Fig. S.12), which suggests that under 0.3m s^{-1} updraft velocities, generation of $s_{\text{max}} > 0.2\%$ at this site is
772 likely. During summer months, the likelihood of surpassing the dry PNSD surface area threshold of $100 \mu\text{m}^2 \text{cm}^{-3}$
773 increases from 10% to 22% (Fig. S.12) due to biogenic SOA formation (e.g., Tunved et al., 2006; Heikkinen et
774 al., 2020), which grows the accumulation mode in the PNSD. Biogenic SOA formation depends on the SOA
775 precursor i.e., BVOC emissions and concentrations. Monoterpene concentrations are highest at SMEAR II in
776 summer (Kontkanen et al., 2016; Hakola et al., 2012) as their emissions are strongly temperature-driven (Guenther
777 et al., 1993). The organic vapor concentration available for co-condensation is therefore also highest in summer,
778 but due to the enhanced surface area, the soluble organic mass is distributed to larger particles dampening the
779 cloud response to co-condensation. However, the monoterpene emission period is longer than just summer, and
780 elevated monoterpene concentrations can be observed throughout the thermal growing season (when the daily
781 average temperature is above 5°C ; Kontkanen et al., 2016; Hakola et al., 2012). Therefore, monoterpene emissions
782 take place also at times when the dry PNSD surface area stays below the $100 \mu\text{m}^2 \text{cm}^{-3}$ threshold.

783 Fig. 6b shows the dry PNSD surface area derived from the long-term PNSD measurements at SMEAR
784 II as a function of temperature. When the ambient temperature exceeds 5°C , the dry PNSD surface area starts to
785 increase with increasing temperature. The dry PNSD surface areas and ambient temperatures (from 8.4 m height;
786 Fig. 1c) from the BAECC simulation period are also shown to highlight the fact that the BAECC sample represents
787 well the long-term statistics of the thermal growing season, providing confidence in the representativity of the
788 BAECC sampling period for this boreal environment. The BAECC samples are color-coded by the modelled
789 ΔCDNC . The highest ΔCDNC (i.e., $\Delta\text{CDNC} > 40\%$) are modeled when the dry PNSD surface areas are below
790 the $100 \mu\text{m}^2 \text{cm}^{-3}$ threshold. Importantly, most of these model scenarios yielding $\Delta\text{CDNC} > 40\%$ coincide with
791 ambient temperatures between 5 and 8°C i.e., at times when the monoterpene concentrations are not at their
792 highest yet sufficient concentrations of organic vapor are still present to cause a large cloud response. It can
793 thereby be concluded that the highest ΔCDNC due to co-condensation can be expected in thermal Spring and Fall.
794 However, due to the seasonality in hygroscopicity and the slightly higher κ in spring and autumn (as opposed to
795 summer; Fig. 6a) the likelihoods of obtaining s_{max} exceeding 0.2% to yield significant ΔCDNC can be somewhat
796 buffered due to hygroscopic growth.

797 Next, the frequency to which the PNSD criteria ($D_2/D_1 < 6$ and $N_1 > 1000 \text{ cm}^{-3}$) are fulfilled in the long-
798 term size distribution measurements is examined. For this purpose, the same 6-year PNSD data set collected at
799 SMEAR II fitted with two log-normal size distributions (Hussein et al., 2005) is utilized. The percentage of times
800 the criteria are met is shown in Fig. 7a. The highest frequencies (30–40% of the time) are observed in April, May
801 and September, which correlates with a high new particle formation (NPF) frequency at the site (Nieminen et al.,
802 2014; Dada et al., 2017). The monthly median size distributions fulfilling the criteria are shown in Fig. 7c. They
803 all clearly exhibit the lack of a Hoppel minimum, similarly to PNSD_{NUM} , and suggest a potentially high impact of
804 newly formed particles on cloud properties through co-condensation. However, future work should focus on
805 understanding how frequently the measured PNSD_{NUM} are actually exposed to droplet activation, which would
806 help us assess the likelihood of large CDNC enhancements taking place in reality. This is particularly important,
807 because NPF typically takes place in sunny, non-cloudy days, which provides time for the PNSD_{NUM} to evolve
808 before exposed to cloud base and subsequent droplet activation. The results again clearly emphasize the need of
809 accurate representation of aerosol size distributions and lifecycle in models (such as other CPMs or global
810 circulation models, GCMs) to account for the impacts of co-condensation and the strong seasonality to be expected
811 in the magnitudes in ΔCDNC .

812

813 **3.5 Expected spatiotemporal variability in the impact of co-condensation on CDNC over the boreal biome**

814

815 In this section the SMEAR II results are compared against a 5-year UKESM1 simulation (see Sect. 2.4; analysis
816 restricted to the boreal biome). While the SMEAR II PNSD data are retrieved at ground level, utilization of the
817 UKESM1 modal parameters (only soluble modes considered) from CB is chosen, because these PNSD log-normal
818 parameters would actually meet the cloud droplet activation scheme in the model. Previous co-condensation
819 parameterization schemes have also been developed to treat the CB PNSD to account for co-condensation
820 (Connolly et al., 2014; Crooks et al., 2018). The monthly averages of the percentage of times the criteria ($D_2/D_1 < 6$
821 and $N_1 > 1000 \text{ cm}^{-3}$) are fulfilled in the boreal grids are shown in Fig. 7b. Here, the Aitken mode geometric mean
822 diameter and total number concentration (D_1 , N_1) and accumulation mode geometric mean diameter (D_2) are
823 obtained from the soluble Aitken and accumulation modal parameters (see Sect. 2.4 for more details regarding
824 the UKESM1 modes). The frequencies, which remain roughly well below 6%, are in general much lower than
825 observed at SMEAR II. This can be explained by the lack of the boundary layer NPF process in the UKESM1
826 simulations (Sect 2.4). Therefore, the UKESM1 results can be taken as the lower estimate. Fig. 7d displays the
827 monthly median PNSD in the boreal grid cells fulfilling the criteria ($D_2/D_1 < 6$ and $N_1 > 1000 \text{ cm}^{-3}$), which are
828 constructed from the soluble Nucleation, soluble Aitken and soluble accumulation mode modal parameters from
829 the UKESM1 simulations when the criteria are fulfilled (criteria only uses soluble Aitken and soluble
830 accumulation modes). The size distributions calculated using these UKESM1 modal parameters are in general
831 less similar to the PNSD_{NUM} than the monthly median SMEAR II size distributions are (Fig. 7c), because they
832 have more distinguished multimodal shapes, which arises from the modal representation of the PNSD. However,
833 they still feature a minor accumulation mode in the presence of a large Aitken mode (with respect to N).

834 The UKESM1 results suggest that a strong spatiotemporal variability in the co-condensation driven
835 ΔCDNC should be expected if this process were to be represented in GCMs. Consistently with the SMEAR II
836 observations (Fig. 7a), spring months stand out as the times when the criteria are most likely to be met, but the
837 other peak in the frequency, expected in September at SMEAR II, cannot be seen. Another interesting feature is

838 the large spatial variability in the frequency. In March and April, a very evident hotspot can be seen in the southern
839 parts of the boreal forest, more precisely in the north of Kazakhstan. When the whole northern hemisphere is
840 displayed, it is clear that the hot spot region extends over Europe during Spring (Fig. S.13) when the conditions
841 favor the formation, growth and survival of small particles (Kerminen et al., 2018) as shown in Fig. S.14 in terms
842 of nucleation mode number concentration. The result therefore suggests high co-condensation potential in areas
843 rich in ultrafine particles. The cloud response of co-condensation in an extended domain covering most of Eurasia
844 could be an interesting follow-up study. However, such a study should incorporate also the condensation of nitric
845 acid and ammonia, the concentrations of which are presumably abundant in the regions, where the co-
846 condensation PNSD criteria are met (Kakavas et al., 2022). As this “Kazakhstan hotspot” is connected to aerosol
847 phenomenology outside the boreal biome, the analysis is not continued further. Another evident springtime hot
848 spot is located in North America, near the Rocky Mountains, but the updraft velocities at the area are not within
849 the desired range ($[0.2, 0.5] \text{ m s}^{-1}$) to yield significant cloud response from co-condensation (Fig. 7b).

850 Aside from these hotspots, it is notable that the overall background of the frequency of the times the
851 criteria are met in the latitude range of $[0, 75]^\circ\text{E}$ increases from $<2\%$ to $2\text{--}6\%$ when moving from March to April.
852 This background stays elevated until June. Smaller hotspots within this area are visible and they correspond to
853 regions known with high sulfur dioxide (SO_2) emissions, such as the Kola peninsula. The Kola peninsula SO_2
854 emissions have shown to trigger NPF events measured at SMEAR I in Finnish Eastern Lapland (e.g., Kyrö et al.,
855 2014). An interesting next step would be to see how Fig. 7b changes with UKESM1 simulations incorporating
856 boundary layer NPF and whether the percentage of times the criteria are met increases to values comparable with
857 the SMEAR II observations and whether the frequency becomes larger also in Fall. Another interesting
858 observation to be made from Fig. 7b is that no significant impact of co-condensation would be expected in
859 UKESM1 in most of Siberia (East and Northeastern Siberia), which can be explained by the lack of nucleation
860 mode particles in the UKESM1 simulations over the region (Fig. S.15).

861 **4 Conclusions**

862
863 This study focuses on the role of the co-condensation of organic vapor and water on warm cloud microphysics in
864 a boreal forest environment. Co-condensation has been proposed as a potentially significant process contributing
865 to the feedbacks between VOC emissions, SOA loadings, cloud formation and climate. Boreal forests account for
866 about a third of the Earth’s forested area and are potentially significant sources of such co-condensing species.

867 First, PARSEC-UFO model is used to perform simulations for the BAECC measurement campaign
868 which took place at the SMEAR II station in Southern Finland during 2014 (Petäjä et al., 2016). The measurement
869 setup during BAECC was very advanced, enabling the initialization of PARSEC-UFO with state-of-the art data
870 describing the ambient aerosol physical and chemical properties. The measurements conducted with the
871 FIGAERO-I-CIMS (e.g., Mohr et al., 2017) are of high importance for this study due to the simultaneous
872 measurements of organic particle and vapor species. These data enable the incorporation of organic vapors from
873 a broad volatility range into the PARSEC-UFO simulations. The previous modeling work on this topic used
874 volatility distributions based on particle-phase measurements only, resulting in overall lower volatility and
875 contributions of semi- and intermediate volatility organic vapor.

876 The results from the PARSEC-UFO simulations reveal that a competition effect exists between the
877 reductions in maximum supersaturations and critical supersaturations needed for aerosol particle activation into

878 cloud droplets when co-condensation is considered. The reductions in critical supersaturations are greater than the
879 reductions in maximum supersaturation, which results in the simulated CDNC enhancements (simulations with
880 co-condensation are compared against simulations without it under same meteorological conditions). The CDNC
881 enhancements are of the order of 20% under realistic updraft velocities (0.1, 0.3, and 1 m s⁻¹) and correspond to
882 reductions of 10–13 nm in the smallest activated dry diameters (~144 to ~128 nm, ~102 to ~88 nm, 72 to ~62 nm
883 for the 0.1, 0.3, and 1 m s⁻¹ updraft scenarios, respectively). The activation of smaller particles into cloud droplets
884 results, as expected, in the formation of more numerous smaller cloud droplets. The critical supersaturation
885 reductions result from the additions of soluble organic mass below cloud base along the simulated air parcels’
886 adiabatic ascents while the reductions in maximum supersaturation are caused by the increasing condensation sink
887 provided by more cloud droplets (the source of supersaturation is fixed as the meteorological conditions between
888 simulations with and without co-condensation are kept constant).

889 The predicted CDNC enhancements are highest for the 0.3 m s⁻¹ updraft velocities and depend on several,
890 at least partly, interlinked parameters (see also Lowe et al., 2019). One parameter affecting the modelled CDNC
891 is the availability of the co-condensable organic vapors, which in turn depends on the updraft velocities, the
892 features of the organic volatility distribution as well as initial temperature and relative humidity. Most organic
893 vapor condenses under the slowest adiabatic ascents and least in the highest due to kinetics. The organic volatility
894 bins spanning from ELVOCs to the lower-volatility IVOCs condense in a similar, updraft-dependent, degree prior
895 reaching the cloud base. Organic vapors of higher volatility involving species such as formic acid condense less
896 efficiently and their condensation is sensitive to the presence of large particles, which are likely to activate
897 regardless of co-condensation. Therefore, small enhancements in particularly SVOC and lower-volatility IVOC
898 concentrations lead to significant enhancements in CDNC, while increases in the most volatile IVOCs and formic
899 acid do not affect CDNC much.

900 The simulations performed with 0.3 m s⁻¹ updrafts are repeated using volatility distributions from
901 previous co-condensation studies (Cappa and Jimenez, 2010; Topping et al., 2013; Crooks et al., 2018). By doing
902 so, the BAEC campaign median CDNC enhancement decreased from 22% to non-significant values. This result
903 is explained by the lower initialization temperature regulating organic vapor availability as well as lower SVOC
904 and IVOC concentrations in previous studies, highlighting the added value of capturing these higher volatility
905 bins within the VBS representations of atmospheric organic species. On the other hand, adding information on
906 the LVOC and ELVOC range do not significantly influence the CDNC enhancements due to co-condensation.

907 The sensitivity of the modelled Δ CDNC to organic vapor concentrations is strongest when high
908 maximum supersaturations ($s_{\max} > 0.2\%$ for the 0.3 m s⁻¹ updraft scenarios) are reached. Such conditions are
909 achieved when the dry PNSD surface area (a proxy for the condensation sink) remains below 100 $\mu\text{m}^2 \text{cm}^{-3}$. Under
910 those conditions, CDNC enhancements exceeding 40% are predicted for conditions in which roughly 1 $\mu\text{g m}^{-3}$ of
911 co-condensable organic vapor is present.

912 Besides the meteorological conditions and the availability of co-condensable vapors, the CDNC
913 enhancements depend critically on the size distribution of the initial aerosol population. Highest CDNC
914 enhancements are generally achieved when the model is initialized with a relatively weak accumulation mode
915 combined with a large nascent ultrafine particle mode with a geometric mean diameter of ca. 40 nm, with no
916 visible Hoppel minimum present in the distribution. Such conditions are observed most frequently in Spring and

September (about 30–40% of the time in years 2012–2017), when new particle formation events take place at SMEAR II.

Further on, UKESM1 simulations (years 2009–2013) are utilized to investigate the potential impact of including the process of co-condensation on droplet formation in this model over the whole boreal biome using the criteria developed from the SMEAR II case to identify most susceptible PNSD conditions. Overall, the UKESM1 PNSD are different from those observed at SMEAR II even when the strict criteria are used to select the ideal PNSD for co-condensation driven enhancements in CDNC. This discrepancy can arise from multiple causes such as the lack of critical aerosol processes (boundary layer new particle formation), but it could also be a common ESM feature arising from the modal representation of PNSD. Nonetheless, aside from two hotspots (one near the Rocky Mountains in North America, one over northern Kazakhstan, which are not analyzed further), the presence of suitable PNSD, as experienced by UKESM1, is most frequent over Fennoscandia and western parts of Siberia in spring, yet the frequencies at which those PNSD are modelled remained much lower than those obtained from the long-term SMEAR II PNSD measurements (2–6% in UKESM1). Perhaps surprisingly, suitable PNSD are never modeled over most of Siberia, suggesting that for the model configuration of UKESM1 used in this study, the process of co-condensation would not be expected to have an influence on droplet formation in this area. This is due to the low concentration of ultrafine particle particles modeled in the area.

In summary, these results highlight the potential significance of co-condensation in pristine boreal environments with a nascent ultrafine particle mode present. Such conditions are met over Fennoscandia and Western parts of Siberia in Spring and to a lesser extent in the Fall, when NPF takes place. For future modelling purposes, it is vital to stress the importance of the accurate representation of PNSD for capturing the role of co-condensation of organics on CDNC enhancements, including appropriate description of boundary layer NPF. Because the modelled CDNC enhancements are so significant, further research focus especially regarding observations of the co-condensation should be targeted in the future to motivate future assessments of co-condensation-driven radiative forcing. Perhaps this work inspires aircraft measurements (of the relevant parameters discussed in this paper) to take place over the Fennoscandia in the future to finally narrow down the importance of co-condensation for the accurate representation of CDNC in GCMs.

Appendix A

The effect of the initialization relative humidity, organic mass accommodation coefficient (α_{org}) and vaporization enthalpy (ΔH_{VAP}) on the modelled CDNC enhancements due to co-condensation are investigated for three different conditions (simulation IDs #13, #55 and #95, respectively; Table S.1). The three conditions were selected as they are representative of low, median and high ΔCDNC simulated during BAECC Table A.1. describes the simulation setup for this sensitivity study.

Table A.1. The simulation setup for studying the sensitivities of initialization RH organic mass accommodation coefficient (α_{org}) and vaporization enthalpy (ΔH_{VAP}) on ΔCDNC is shown. Three simulation IDs are selected from the BAECC campaign (#13, #55 and #95, respectively; Table S.1) and three simulation sets (for varying initialization RH, α_{org} and ΔH_{VAP} , respectively) are performed for each ID with and without co-condensation. The initial temperature, aerosol chemical composition and PNSD vary between the different IDs, and are taken from Table S.1. A fixed updraft velocity of 0.3 m s^{-1} is applied for all the different simulations.

Set	Co-condensation	Initialization RH [%]	α_{org}	ΔH_{VAP} [kJ mol ⁻¹]
1a	OFF	[60, 80, 90, 95, 99]	1	150

1b	ON	[60, 80, 90, 95, 99]	1	150
2a	OFF	90	[0, 0.2, 0.4, 0.6, 0.8, 1.0]	150
2b	ON	90	[0, 0.2, 0.4, 0.6, 0.8, 1.0]	150
3a	OFF	90	1	[80, 100, 120, 150, 200]
3b	ON	90	1	[80, 100, 120, 150, 200]

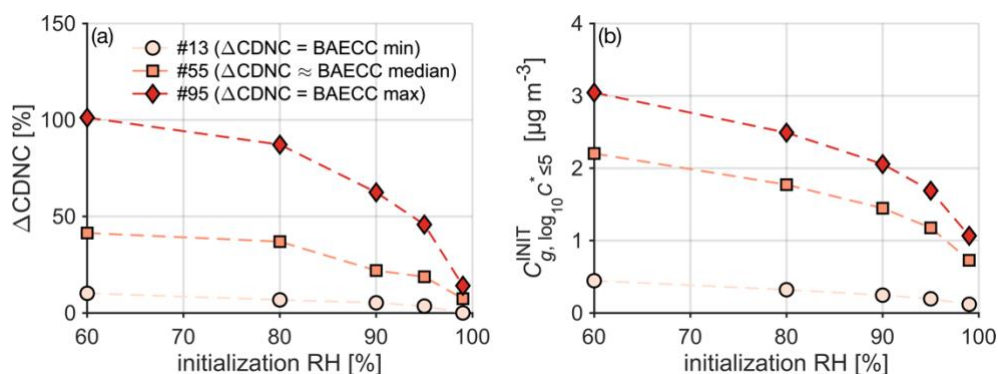
958

959 The initialization RH affects the availability of organic vapor for co-condensation: when PARSEC-UFO is
960 initialized under high RH ($\sim >95\%$), most organic vapor is scavenged at initial conditions causing negligible
961 enhancements in CDNC. On the other hand, if the initialization RH is lower ($<90\%$), less organic vapor is
962 scavenged at initial conditions, and the modeled Δ CDNC are greater (Fig. A.1). By varying α_{org} , the effect of the
963 assumption of ideality has on the projected CDNC enhancements is probed. For simplicity, the mass
964 accommodation coefficient for organics (α_{org}) is set to be constant across the volatility bins. By reducing α_{org}
965 from 1 to 0.8, the condensation of organics reduces. However, this impacts CDNC only in the simulation ID #95
966 (Fig. A.2; CDNC reduces from $\sim 62\%$ to 55%), i.e., simulation with the highest Δ CDNC. When $\alpha_{\text{org}} < 0.4$, also
967 the simulation ID #55 shows a reduction in the modeled Δ CDNC as it drops from $\sim 22\%$ to $\sim 15\%$. The selection
968 of the enthalpy of vaporization for organics does not affect Δ CDNC (Fig. A.3). Over all, the initial relative
969 humidity plays the most critical role out of the three parameters considered here (RH, α_{org} and ΔH_{VAP}), on the
970 modelled Δ CDNC.

971

972

973



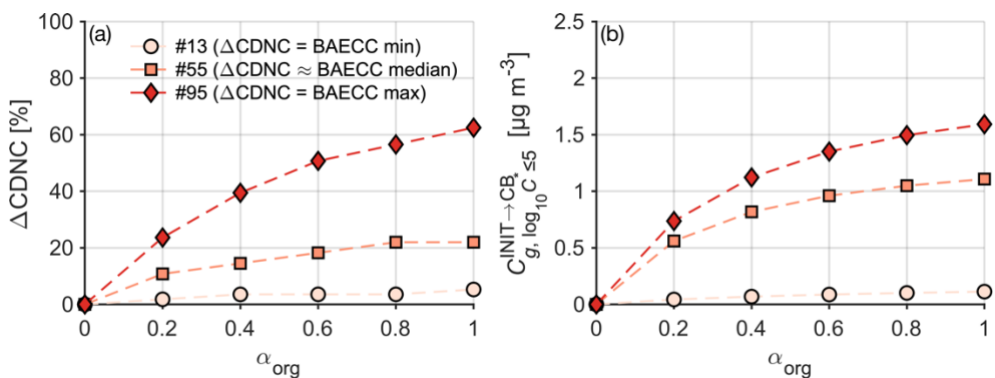
974

975

976 **Figure A.1** The modelled CDNC enhancements as function of initialization RH ranging from 60% to 99%
977 (indicated with different colors) for each simulation ID are shown, respectively. The initialization temperature
978 and pressure are fixed to values shown in Table S.1. and only the volatility bins $\log_{10} C^* \leq 5$ are included, which
979 is motivated e.g., by Fig. 4. The simulations are performed with an updraft velocity of 0.3 m s^{-1} . The markers with
980 the lightest color refer to the BAECC simulation, where co-condensation influenced Δ CDNC negligibly (ID #13,
981 Δ CDNC = 3%), the orange markers to the BAECC median Δ CDNC (ID #55), and the red markers represent a
982 simulation, where the modelled Δ CDNC was greatest (ID #95, Δ CDNC = 75%). Δ CDNC is calculated 50 m above
983 CB based on critical radii, similarly to the study.

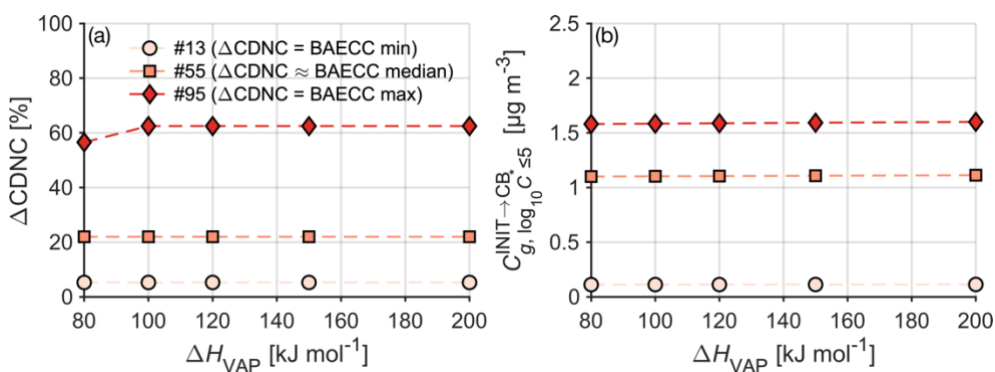
984

985



986
 987 **Figure A.2** The modelled CDNC enhancements as function of mass accommodation coefficient for organics (α_{org})
 988 ranging from zero to one. The colorings and presented simulations are same as in Fig. A.1.
 989

990



991
 992
 993 **Figure A.3** The modelled CDNC enhancements as function of vaporization enthalpy for organics (ΔH_{VAP}) ranging
 994 from zero to one. The colorings and presented simulations are same as in Fig. A.1.
 995

996

997 **Data availability**

998 The PARSEC-UFO input and outputs for reproducing the figures will be available on the Bolin Centre database.

999

1000 **Competing interests**

1001 The authors have the following competing interests: Some authors are members of the editorial board of
1002 Atmospheric Chemistry and Physics. The peer-review process will be guided by an independent editor. One or
1003 more authors have received funding from European Union's Horizon 2020 research and innovation programme,
1004 European Research Council, Knut and Alice Wallenberg foundation, Academy of Finland and US Department of
1005 Energy, UK Natural Environment Research Council (NERC), and/or support from ACTRIS Translational Access
1006 and ACTRIS-HY. The authors have no other competing interests to declare.

1007 **Author contributions**

1008 LH, IR, DGP and CM conceptualized the idea of the study and designed the simulations. LH prepared the
1009 PARSEC-UFO input data, performed the PARSEC-UFO simulations, analyzed the simulation outputs, made the
1010 majority of the figures and wrote the manuscript with contributions from the coauthors. TP designed and led the
1011 BAECC campaign. CM performed the FIGAERO-I-CIMS measurements, WH processed and delivered the
1012 FIGAERO-I-CIMS data and gave input on the volatility distribution calculation. RR assisted LH with the
1013 radiosonde data, provided the hygroscopicity seasonal cycle data and contributed to the PARSEC-UFO
1014 description writing. ET and DGP performed the UKESM1 simulations and DGP designed and processed the data
1015 for analysis input parameters to droplet activation parameterization. DGP and PB created PARSEC and extended
1016 it to include UFO, provided documentation for PARSEC-UFO and contribution to description. SB visualized the
1017 UKESM1 data, assisted LH with FORTRAN programming and gave input on the data interpretation.

1018 **Acknowledgements**

1019 We gratefully acknowledge Samuel Lowe for developing the unified framework for organics onto the ICPM
1020 (Lowe, 2020), the useful discussions, code and support. We acknowledge Ellie Duncan for useful discussions and
1021 support regarding the UKESM1 data and Megan Haslum for their documentation on PARSEC-UFO Köhler terms.
1022 We acknowledge Pasi Aalto and SMEAR II staff for their efforts during the BAECC campaign. We thank Dmitri
1023 Moisseev, Federico Bianchi and Annica Ekman for useful discussions. We acknowledge the Atmospheric
1024 Radiation Measurement (ARM) Program for their inputs during BAECC, the interpolated radiosonde data were
1025 obtained from the ARM Program sponsored by the U.S. Department of Energy, Office of Science, Office of
1026 Biological and Environmental Research, Climate and Environmental Sciences Division. We acknowledge use of
1027 the Monsoon2 system, a collaborative facility supplied under the Joint Weather and Climate Research Programme,
1028 a strategic partnership between the Met Office and the Natural Environment Research Council. We also thank all
1029 the people responsible for the development of UKESM1. DGP would like to extend a personal thanks to Dr
1030 Alistair Sellar, who provided support for the configuration of the UKESM1 simulations performed as part of the
1031 AeroCom GCM Trajectory experiment on which these simulations are based.

1032 **Funding**

1033 Financial support from the European Union's Horizon 2020 research and innovation programme (project FORCeS
1034 under grant agreement No 821205, project FOCI under grant agreement No101056783, project CRiceS under
1035 grant agreement No 101003826), European Research Council (Consolidator grant INTEGRATE No 865799,
1036 starting grant CHAPAs No 850614), and Knut and Alice Wallenberg foundation (Wallenberg Academy
1037 Fellowship projects AtmoRemove No 2015.0162 and CLOUDFORM No 2017.0165), Academy of Finland via a
1038 Flagship programme for Atmospheric and Climate Competence Center (ACCC, No 337549) and projects No
1039 353386, 334792, 340791, 325681 are gratefully acknowledged. The BAECC campaign was supported by US
1040 Department of Energy (Petäjä, No DE-SC0010711) and additional measurements were supported via ACTRIS
1041 Transnational Access. University of Helsinki is acknowledged for supporting the SMEAR II station via ACTRIS-
1042 HY. DGP and PB acknowledge support from Natural Environment Research Council (NERC) grant no.
1043 NE/W001713/1 for the creation of the Pseudo-Adiabatic bin-microphysics university of Exeter Cloud parcel
1044 model (PARSEC) and for adding Unified Framework for Organics (UFO) to PARSEC to create PARSEC-UFO.
1045 ET acknowledges support from NERC GW4+ grant no. NE/L002434/1 and DGP from NERC grant no.

1046 NE/W001713/1 for developments to the UKESM1 activation scheme and configuration of the UKSEM1
1047 simulations.

1048
 1049
 1050
 1051
 1052
 1053
 1054
 1055

Tables

Table 1 Overview of the PARSEC-UFO simulation input parameters that remain unchanged in all of the simulation sets conducted with or without co-condensation. The updraft velocities, organic volatility distributions and organic vapor concentrations that change between simulation sets are reported in Table 2 together with the median model outputs. The time series of these model input data are shown in Fig.1. All the modelling scenarios are initiated at 90% relative humidity.

Parameter	Min	Max	Median
Aitken mode number conc. N_1 [cm^{-3}] ^a	160	12 316	1491
Accumulation mode number conc. N_2 [cm^{-3}] ^a	44	2 433	560
Aitken mode geometric mean dry diameter D_1 [nm] ^a	7.1	71.0	23.8
Accumulation mode geometric mean dry diameter D_2 [nm] ^a	62.6	201.9	115.3
Geom. standard deviation of Aitken mode σ_1 ^a	1.50	2.08	1.75
Geom. standard deviation of accumulation mode σ_2 ^a	1.33	2.06	1.75
Number of PNSD size bins	400	400	400
Organic mass fraction f_{Org} [%] ^b	25	84	68
Ammonium sulfate mass fraction f_{AS} [%] ^c	12	75	32
Initial T [K] ^d	271	295	279
Initial p [hPa]	980	980	980
Initial RH [%]	90	90	90
Mass accommodation coefficient α	1	1	1
Vaporization enthalpy for organics ΔH_{vap} [kJ mol^{-1}] ^e	150	150	150
Effective soluble fraction of organics	1	1	1
Surface tension γ [mN m^{-1}]	72.8	72.8	72.8

1056
 1057
 1058
 1059
 1060
 1061
 1062

^a Retrieved from fits assigned onto the measured aerosol size distributions (Aalto et al., 2001) using a fitting algorithm by Hussein et al. (2005).

^b Retrieved from aerosol chemical composition measurements (Heikkinen et al., 2020).

^c $f_{\text{AS}} = 1 - f_{\text{Org}}$

^d Retrieved from radio soundings (ARM Data Center, 2014). The temperatures shown were recorded when the relative humidity measured by the radiosonde reached 90%, i.e., the initial relative humidity used for the adiabatic ascents.

^e Note that in the volatility distribution construction (offline from PARSEC) the ΔH_{vap} is temperature-adjusted following Epstein et al. (2010).

1063 **Table 3** Overview of the PARSEC-UFO simulation output for the no co-condensation (noCC) and co-
 1064 condensation (CC with F volatility distribution) simulations performed using varying updraft velocities.

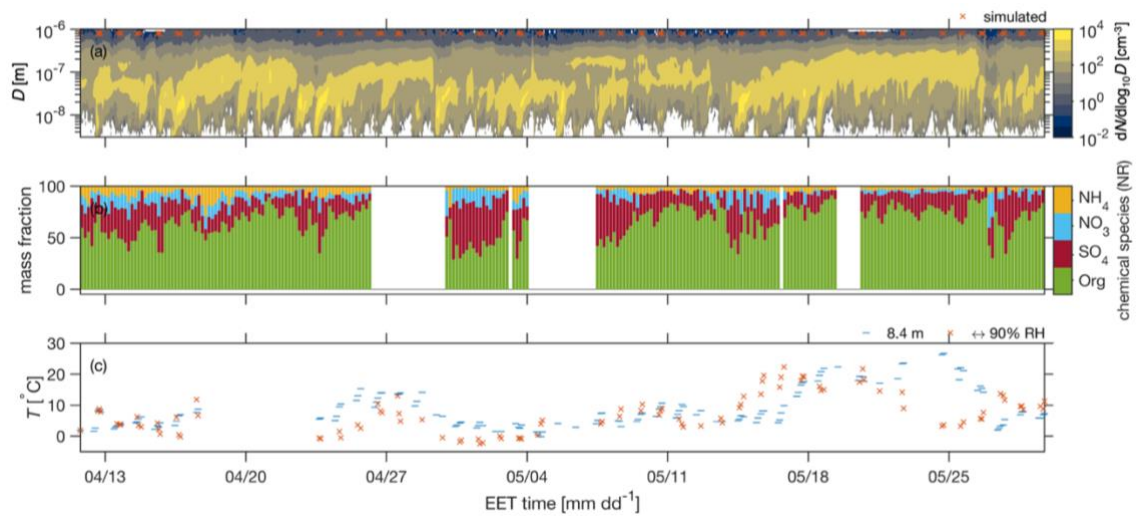
Parameter	Median		
Updraft velocity w [m s ⁻¹] ^a	0.1	0.3	1.0
Parcel displacement before CB [m]	190	190	190
Cloud droplet number conc. CDNC _{noCC} [cm ⁻³] ^b	158	292	523
Cloud droplet number conc. CDNC _{CC} [cm ⁻³] ^b	186	400	618
CDNC enhancement Δ CDNC [%] ^b	15.6	22.1	18.9
Maximum supersaturation s_{\max}^{noCC} [%]	0.14	0.24	0.40
Maximum supersaturation s_{\max}^{CC} [%]	0.14	0.22	0.38
Smallest activated dry radius r_{noCC}^* [nm]	72	51	36
Smallest activated dry radius r_{CC}^* [nm]	64	44	31
Initial organic vapor conc. $\sum C_g^{\text{INIT}}$ [$\mu\text{g m}^{-3}$]	22.05	2.05	2.05
Organic vapor condensed below cloud base $\sum C_g^{\text{INIT}} - \sum C_g^{\text{CB}}$ [$\mu\text{g m}^{-3}$]	1.82	1.41	0.55
Fraction of organic vapor condensed below cloud base $\Delta C_g^{\text{INIT} \rightarrow \text{CB}}$ [%]	91	70	28

1065
 1066
 1067
 1068
 1069
 1070

^a Model input parameters crucial for understanding the differences between the co-condensation simulation model outputs.

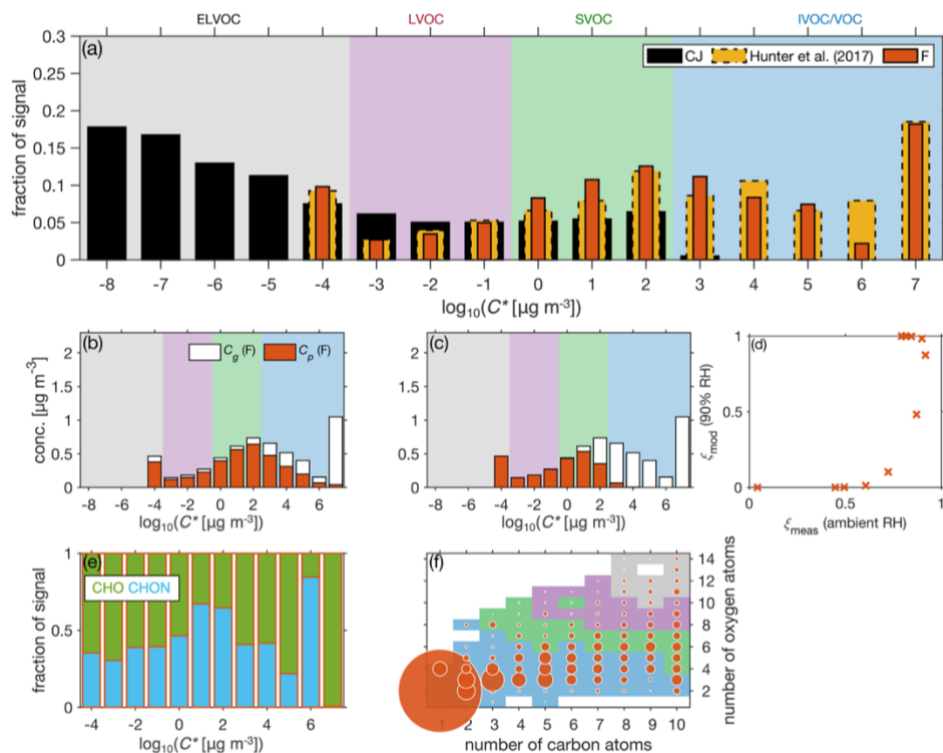
^b The CDNC represent the integrated number concentration in size bins exceeding the critical radius in wet size at 50 meters above cloud base (CB).

1071 **Figures**
1072



1073
1074
1075
1076
1077
1078
1079
1080

Figure 1 (a) Time-series of the particle number size distribution in the time period of interest during BAECC. The time points used for the PARSEC-UFO initialization are shown as red/orange crosses. (b) The non-refractory (NR) chemical composition of sub-micrometer aerosol particles for the same time period. (c) The time series of ambient temperature near ground level (8.4 m a.g.l.) is shown in blue and the PARSEC-UFO initialization temperature corresponding to RH = 90% from the interpolated radiosonde data product is shown in orange. The subpanels have a common x-axis representing the East European winter time (UTC+2).



1082

1083

1084

Figure 2 (a) The normalized volatility distributions ($C_g + C_p$) from Cappa and Jimenez (2010; CJ) and the BAECC FIGAERO-

I-CIMS measurements (F) using the modified Li et al. (2016) molecular formulae-based parameterizations. A volatility

distribution from Hunter et al. (2017) constructed from the BEACHON-RoMBAS measurement campaign is shown by the

dashed bars. The volatility ranges for ELVOC, LVOC, SVOC and IVOC/VOC are shown in color scales. These C^* limits

apply throughout the paper. (b–c) The partitioning predicted based on the FIGAERO-I-CIMS gas- and particle-phase

measurements and the PARSEC-UFO, respectively. The PARSEC-UFO partitioning corresponds to 90% RH while the

ambient observation is under ambient RH. (d) A scatterplot drawn between the FIGAERO-I-CIMS derived partitioning

coefficients (ζ_{meas}) and PARSEC-UFO-derived coefficients (ζ_{mod}) for the 12 different volatility bins. Panels (e–f) represent the

gas phase molecular composition from the FIGAERO-I-CIMS: panel (e) the distribution between organic nitrates and non-

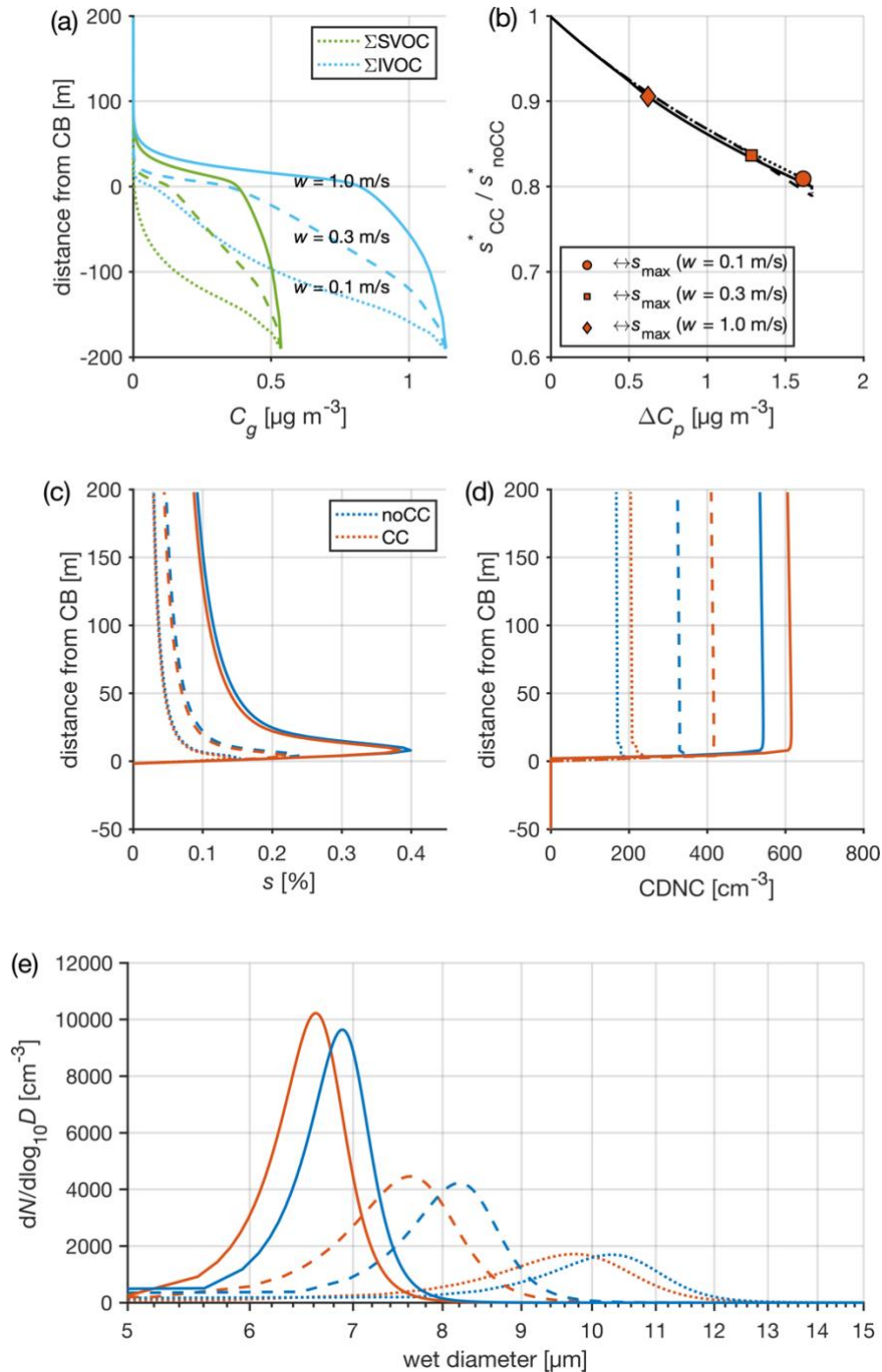
nitrates and panel (f) the degree of oxygenation in the form of oxygen and carbon numbers. The marker size in panel f

corresponds to the concentration of signal for the given n_C and n_O combination.

1095

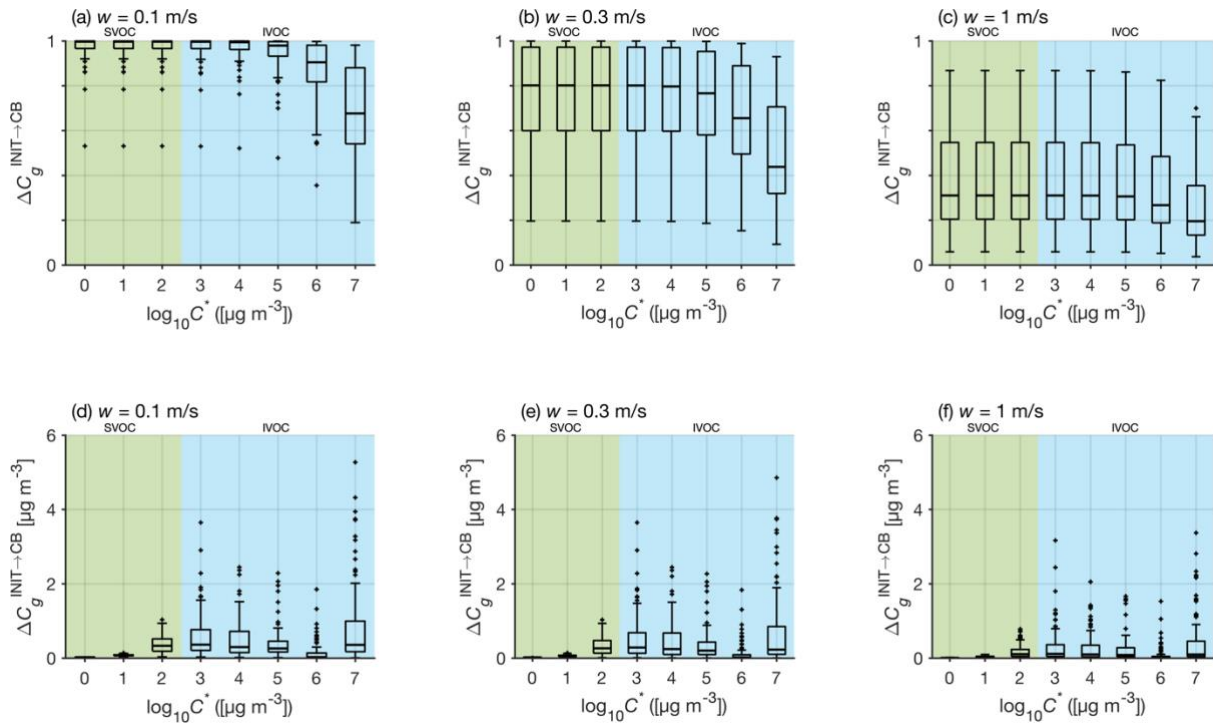
1096

1097



1098
 1099
 1100
 1101
 1102
 1103
 1104
 1105
 1106
 1107
 1108
 1109
 1110
 1111

Figure 3 A summary of simulated cloud microphysics on May 11, 13:37 EET during the BAECC campaign. Simulations are performed both with and without organic condensation (red and blue lines, respectively) for three different updraft velocities (see line styles from panel a). The initial temperature is 279 K, pressure 980 hPa and RH is 90%. (a) The concentration of SVOCs and IVOCs in the gas phase as a function of distance from cloud base (CB). SVOCs have $\log_{10}C^* = [0, 2]$ and IVOCs $\log_{10}C^* = [3, 7]$ under 279 K. (b) The relative change in critical supersaturation (s^*) between noCC and CC simulations, as a function of soluble mass added along the ascent by condensing organics in the simulations, where co-condensation is enabled. The data are shown for a particle with a dry diameter of 147 nm at PARSEC-UFO initialization. The markers represent the reductions at the time when maximum supersaturation (s_{\max}) was reached. (c–d) The evolution of the s_{\max} and CDNC with altitude, respectively. (e) The droplet spectra 50 meters above CB. Size bins exceeding the critical diameter as predicted by Köhler theory are calculated as cloud droplets. The red lines are obtained with F volatility distributions (Fig. 2a). The line type specifications in panels d–e follow those shown in panel a and the colors used in panels d–e are documented in the panel c legend.



1112

1113

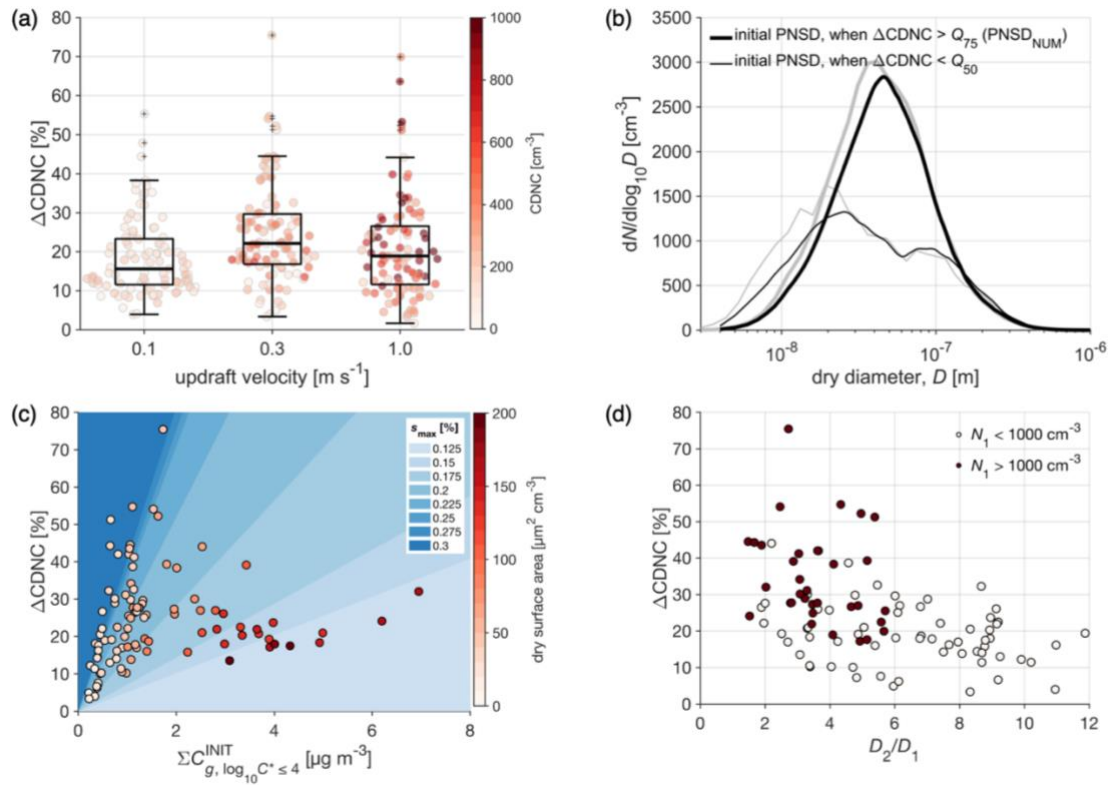
1114

1115

1116

1117

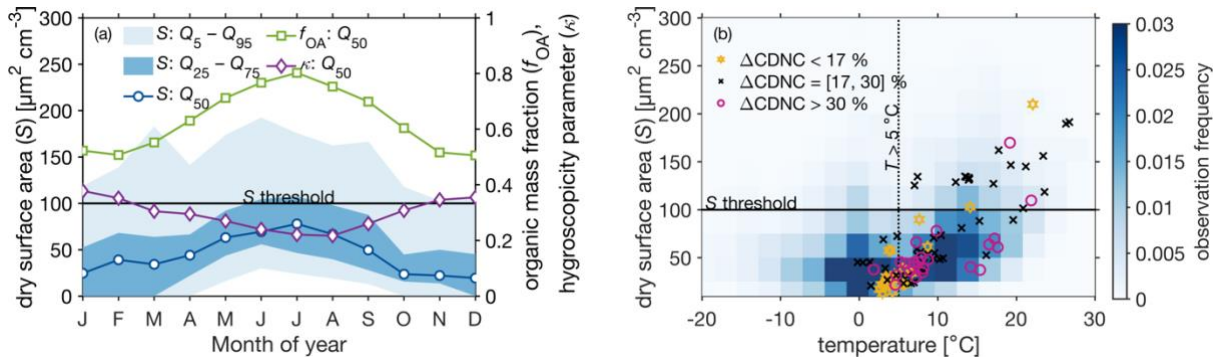
Figure 4 Box plots showing the fractions (a–c) and absolute concentrations (d–f) of organic vapor condensed below cloud base per volatility bin for the 0.1, 0.3 and 1.0 m s⁻¹ updraft scenarios, respectively. The shaded backgrounds reflect SVOC (green) and IVOC/VOC (blue) volatility ranges under PARSEC-UFO initialization temperature.



1118
 1119
 1120
 1121
 1122
 1123
 1124
 1125
 1126
 1127
 1128
 1129
 1130
 1131
 1132
 1133

Figure 5 (a) Box plots showing the predicted ΔCDNC (using F volatility distributions) due to co-condensation in the three different modelling scenarios (0.1, 0.3 and 1.0 m s^{-1} updrafts). The colorful markers represent CDNC (without accounting for co-condensation) in form of a swarmplot. The median (Q_{50}) ΔCDNC yielded using the CJ distribution are shown in Fig. S.7. (b) The median initial dry size distributions calculated from the simulations exceeding the 75th percentile in ΔCDNC ($>Q_{75}$; thick lines) and remaining below the ΔCDNC median ($<Q_{50}$; thin lines), respectively. The PNSD medians are calculated by taking a median of the PNSD calculated using the log-normal parameters from both sets of simulations (in black) and from the measurement data (in grey). The data are shown for the simulation performed with a 0.3 m s^{-1} updraft. (c) The relationship between the modeled ΔCDNC and the initial organic vapor concentration within the $\log_{10}C^*$ range from -4 to 4 ($C_{g, -4:4}^{\text{INIT}}$). The marker color-coding represents the initial dry size distribution surface area (S). The plot background is colored with the modeled maximum supersaturations (s_{max}). These are calculated from s_{max} binned ΔCDNC vs $C_{g, -4:4}^{\text{INIT}}$ linear fit 90% confidence intervals (CI; area between CI is colored). The figure shows that S anticorrelates with s_{max} (see Eq. 3). The data are shown for the simulations performed with a 0.3 m s^{-1} updraft only. (d) The figure evaluates how well the simple criteria ($D_2/D_1 < 6$ and $N_1 > 1000 \text{ cm}^{-3}$) works on the PARSEC-UFO simulations.

1134



1135

1136

1137

1138

1139

1140

1141

1142

1143

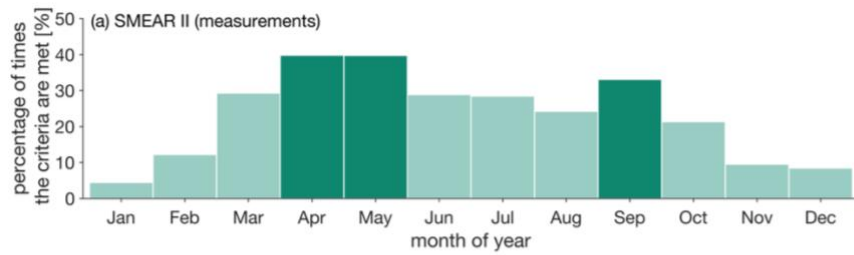
1144

1145

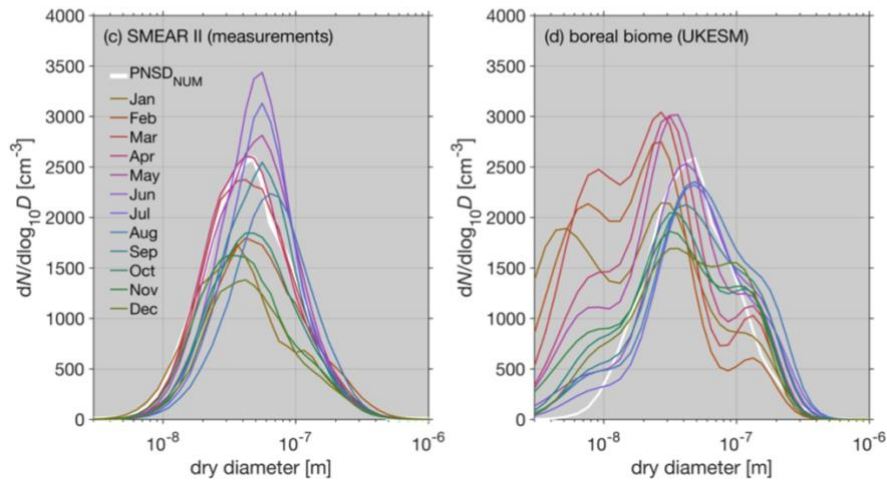
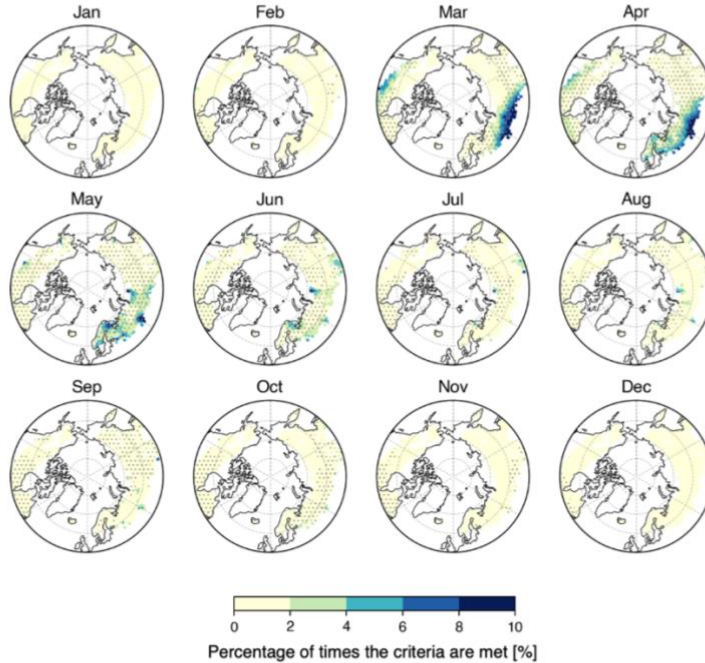
1146

1147

Figure 6 (a) The seasonal cycle of the dry aerosol size distribution surface area (S) calculated from the long-term aerosol size distribution observations (2012–2017; left y-axis), where the markers represent the median values, the darkest shading the interquartile range and the lighter shading the area between the 5th and 95th percentiles. The panel also contains the median seasonal cycles of organic mass fraction and the κ hygroscopicity parameter compiled from the same long-term period (right y-axis). The green horizontal line refers to the dry surface area threshold of $100 \mu\text{m}^2 \text{cm}^{-3}$ from Fig. 5, under which the greatest ΔCDNC are modeled using the BAEC data. (b) A density plot showing the observations of S under different ambient temperatures during the 2012–2017 long-term period. The S threshold of $100 \mu\text{m}^2 \text{cm}^{-3}$ is again shown with the horizontal green line. The vertical dashed green line is a rough estimate for the start of the thermal growing season, which also refers to the starting point of the majority of the BVOC emissions. The markers show the PARSEC-UFO simulation data color-coded with the associated ΔCDNC (simulations yielding the ΔCDNC below the 25th percentile are shown in blue, simulations yielding ΔCDNC above the 75th percentile in red and the simulations between those limits are shown in white).



(b) boreal biome monthly medians (UKESM)



1148
1149
1150
1151
1152
1153
1154
1155
1156
1157
1158
1159
1160

Figure 7 (a) Percentage of times the criteria ($D_2/D_1 < 6$ and $N_1 > 1000 \text{ cm}^{-3}$) are met at SMEAR II between the 2012–2017 measurement period. D_2 , D_1 and N_1 are attained from bimodal fits calculated for the measured PNSD using the Hussein et al. (2005) algorithm. (b) The percentage of times the criteria are met in a 2009–2013 UKESM1 simulation. D_2 , D_1 and N_1 are the log-normal parameters representing the soluble accumulation mode and soluble Aitken modes. The gray markers refer to boreal grid cells, where the median updraft velocity at cloud base is between 0.2 and 0.5 m s^{-1} . (c–d) Monthly median size distributions from the long-term PNSD measurements at SMEAR II and UKESM1 simulation, respectively. The UKESM1 size distributions are calculated from the log-normal PNSD parameters for nucleation, soluble Aitken and soluble accumulation modes assuming geometric standard deviations of $\sigma = 1.59$ for nucleation and soluble Aitken modes and $\sigma = 1.4$ for the soluble accumulation mode. The soluble coarse mode is not included in the analysis.

1161 **References**

- 1162 Aalto, P., Hämeri, K., Becker, E., Weber, R., Salm, J., Mäkelä, J. M., Hoell, C., O’ Dowd, C. D.,
 1163 Hansson, H.-C., Väkevä, M., Koponen, I. K., Buzorius, G., and Kulmala, M.: Physical characterization
 1164 of aerosol particles during nucleation events, *Tellus B: Chemical and Physical Meteorology*, 53, 344–
 1165 358, <https://doi.org/10.3402/tellusb.v53i4.17127>, 2001.
- 1166 Abdul-Razzak, H. and Ghan, S. J.: A parameterization of aerosol activation: 2. Multiple aerosol types,
 1167 *Journal of Geophysical Research: Atmospheres*, 105, 6837–6844,
 1168 <https://doi.org/10.1029/1999JD901161>, 2000.
- 1169 Äijälä, M., Heikkinen, L., Fröhlich, R., Canonaco, F., Prévôt, A. S. H., Junninen, H., Petäjä, T.,
 1170 Kulmala, M., Worsnop, D., and Ehn, M.: Resolving anthropogenic aerosol pollution types –
 1171 deconvolution and exploratory classification of pollution events, *Atmospheric Chemistry and Physics*,
 1172 17, 3165–3197, <https://doi.org/10.5194/acp-17-3165-2017>, 2017.
- 1173 Allan, J. D., Alfarra, M. R., Bower, K. N., Coe, H., Jayne, J. T., Worsnop, D. R., Aalto, P. P., Kulmala,
 1174 M., Hyötyläinen, T., Cavalli, F., and Laaksonen, A.: Size and composition measurements of
 1175 background aerosol and new particle growth in a Finnish forest during QUEST 2 using an Aerodyne
 1176 Aerosol Mass Spectrometer, *Atmos. Chem. Phys.*, 6, 315–327, [https://doi.org/10.5194/acp-6-315-](https://doi.org/10.5194/acp-6-315-2006)
 1177 2006, 2006.
- 1178 AeroCom: <https://aerocom.met.no/>, last access: 21 November 2022.
- 1179 ARM Data Center: Atmospheric Radiation Measurement (ARM) user facility. 2014, updated hourly.
 1180 Interpolated Sonde (INTERPOLATEDSONDE). 2014-04-01 to 2014-07-01, ARM Mobile Facility
 1181 (TMP) U. of Helsinki Research Station (SMEAR II), Hyytiälä, Finland; AMF2 (M1). Compiled by M.
 1182 Jensen, S. Giangrande, T. Fairless and A. Zhou., 2014.
- 1183 Artaxo, P., Hansson, H.-C., Andreae, M. O., Bäck, J., Alves, E. G., Barbosa, H. M. J., Bender, F.,
 1184 Bourtsoukidis, E., Carbone, S., Chi, J., Decesari, S., Després, V. R., Ditas, F., Ezhova, E., Fuzzi, S.,
 1185 Hasselquist, N. J., Heintzenberg, J., Holanda, B. A., Guenther, A., Hakola, H., Heikkinen, L.,
 1186 Kerminen, V.-M., Kontkanen, J., Krejci, R., Kulmala, M., Lavric, J. V., Leeuw, G. de, Lehtipalo, K.,
 1187 Machado, L. A. T., McFiggans, G., Franco, M. A. M., Meller, B. B., Morais, F. G., Mohr, C., Morgan,
 1188 W., Nilsson, M. B., Peichl, M., Petäjä, T., Praß, M., Pöhlker, C., Pöhlker, M. L., Pöschl, U., Randow,
 1189 C. V., Riipinen, I., Rinne, J., Rizzo, L. V., Rosenfeld, D., Dias, M. A. F. S., Sogacheva, L., Stier, P.,
 1190 Swietlicki, E., Sörgel, M., Tunved, P., Virkkula, A., Wang, J., Weber, B., Yáñez-Serrano, A. M., Zieger,
 1191 P., Mikhailov, E., Smith, J. N., and Kesselmeier, J.: Tropical and Boreal Forest – Atmosphere
 1192 Interactions: A Review, *Tellus B: Chemical and Physical Meteorology*, 74, 24–163,
 1193 <https://doi.org/10.16993/tellusb.34>, 2022.
- 1194 Barahona, D., West, R. E. L., Stier, P., Romakkaniemi, S., Kokkola, H., and Nenes, A.:
 1195 Comprehensively accounting for the effect of giant CCN in cloud activation parameterizations,
 1196 *Atmospheric Chemistry and Physics*, 10, 2467–2473, <https://doi.org/10.5194/acp-10-2467-2010>,
 1197 2010.
- 1198 Bardakov, R., Riipinen, I., Krejci, R., Savre, J., Thornton, J. A., and Ekman, A. M. L.: A Novel
 1199 Framework to Study Trace Gas Transport in Deep Convective Clouds, *Journal of Advances in*
 1200 *Modeling Earth Systems*, 12, e2019MS001931, <https://doi.org/10.1029/2019MS001931>, 2020.
- 1201 Barley, M., Topping, D. O., Jenkin, M. E., and McFiggans, G.: Sensitivities of the absorptive
 1202 partitioning model of secondary organic aerosol formation to the inclusion of water, *Atmos. Chem.*
 1203 *Phys.*, 9, 2919–2932, <https://doi.org/10.5194/acp-9-2919-2009>, 2009.
- 1204 Bellouin, N., Quaas, J., Gryspeerdt, E., Kinne, S., Stier, P., Watson-Parris, D., Boucher, O., Carslaw,
 1205 K. S., Christensen, M., Daniou, A.-L., Dufresne, J.-L., Feingold, G., Fiedler, S., Forster, P., Gettelman,
 1206 A., Haywood, J. M., Lohmann, U., Malavelle, F., Mauritsen, T., McCoy, D. T., Myhre, G.,
 1207 Mülmenstädt, J., Neubauer, D., Possner, A., Rügenstein, M., Sato, Y., Schulz, M., Schwartz, S. E.,
 1208 Sourdeval, O., Storelvmo, T., Toll, V., Winker, D., and Stevens, B.: Bounding Global Aerosol

- 1209 Radiative Forcing of Climate Change, *Reviews of Geophysics*, 58, e2019RG000660,
1210 <https://doi.org/10.1029/2019RG000660>, 2020.
- 1211 Boucher, O., Randall, D., Artaxo, P., Bretherton, C., Feingold, G., Forster, P., Kerminen, V.-M.,
1212 Kondo, Y., Liao, H., Lohmann, U., Rasch, P., Satheesh, S. K., Sherwood, S., Stevens, B., Zhang, X.
1213 Y., Stocker, T. F., Qin, D., Plattner, G.-K., Tignor, M., Allen, S. K., Boschung, J., Nauels, A., Xia, Y.,
1214 Bex, V., and Midgley, P. M.: Clouds and Aerosols. In: *Climate Change 2013: The Physical Science
1215 Basis. Contribution of Working Group I to the Fifth Assessment Report of the Intergovernmental Panel
1216 on Climate Change*, Cambridge University Press, 2013.
- 1217 Canagaratna, M. r., Jayne, J. t., Jimenez, J. l., Allan, J. d., Alfarra, M. r., Zhang, Q., Onasch, T. b.,
1218 Drewnick, F., Coe, H., Middlebrook, A., Delia, A., Williams, L. r., Trimborn, A. m., Northway, M. j.,
1219 DeCarlo, P. f., Kolb, C. e., Davidovits, P., and Worsnop, D. r.: Chemical and microphysical
1220 characterization of ambient aerosols with the aerodyne aerosol mass spectrometer, *Mass
1221 Spectrometry Reviews*, 26, 185–222, <https://doi.org/10.1002/mas.20115>, 2007.
- 1222 Cappa, C. D.: A model of aerosol evaporation kinetics in a thermodenuder, *Atmos. Meas. Tech.*, 3,
1223 579–592, <https://doi.org/10.5194/amt-3-579-2010>, 2010.
- 1224 Cappa, C. D. and Jimenez, J. L.: Quantitative estimates of the volatility of ambient organic aerosol,
1225 *Atmos. Chem. Phys.*, 10, 5409–5424, <https://doi.org/10.5194/acp-10-5409-2010>, 2010.
- 1226 Carslaw, K. S., Lee, L. A., Reddington, C. L., Pringle, K. J., Rap, A., Forster, P. M., Mann, G. W.,
1227 Spracklen, D. V., Woodhouse, M. T., Regayre, L. A., and Pierce, J. R.: Large contribution of natural
1228 aerosols to uncertainty in indirect forcing, *Nature*, 503, 67–71, <https://doi.org/10.1038/nature12674>,
1229 2013.
- 1230 Cerully, K. M., Raatikainen, T., Lance, S., Tkacik, D., Tiitta, P., Petäjä, T., Ehn, M., Kulmala, M.,
1231 Worsnop, D. R., Laaksonen, A., Smith, J. N., and Nenes, A.: Aerosol hygroscopicity and CCN
1232 activation kinetics in a boreal forest environment during the 2007 EUCAARI campaign, *Atmospheric
1233 Chemistry and Physics*, 11, 12369–12386, <https://doi.org/10.5194/acp-11-12369-2011>, 2011.
- 1234 Connolly, P. J., Topping, D. O., Malavelle, F., and McFiggans, G.: A parameterisation for the
1235 activation of cloud drops including the effects of semi-volatile organics, *Atmos. Chem. Phys.*, 14,
1236 2289–2302, <https://doi.org/10.5194/acp-14-2289-2014>, 2014.
- 1237 Crooks, M., Connolly, P., and McFiggans, G.: A parameterisation for the co-condensation of semi-
1238 volatile organics into multiple aerosol particle modes, *Geosci. Model Dev.*, 11, 3261–3278,
1239 <https://doi.org/10.5194/gmd-11-3261-2018>, 2018.
- 1240 Dada, L., Paasonen, P., Nieminen, T., Buenrostro Mazon, S., Kontkanen, J., Peräkylä, O., Lehtipalo,
1241 K., Hussein, T., Petäjä, T., Kerminen, V.-M., Bäck, J., and Kulmala, M.: Long-term analysis of clear-
1242 sky new particle formation events and nonevents in Hyytiälä, *Atmos. Chem. Phys.*, 17, 6227–6241,
1243 <https://doi.org/10.5194/acp-17-6227-2017>, 2017.
- 1244 Daumit, K. E., Kessler, S. H., and Kroll, J. H.: Average chemical properties and potential formation
1245 pathways of highly oxidized organic aerosol, *Faraday Discuss.*, 165, 181–202,
1246 <https://doi.org/10.1039/C3FD00045A>, 2013.
- 1247 Donahue, N. M., Robinson, A. L., Stanier, C. O., and Pandis, S. N.: Coupled Partitioning, Dilution, and
1248 Chemical Aging of Semivolatile Organics, *Environ. Sci. Technol.*, 40, 2635–2643,
1249 <https://doi.org/10.1021/es052297c>, 2006.
- 1250 Donahue, N. M., Epstein, S. A., Pandis, S. N., and Robinson, A. L.: A two-dimensional volatility basis
1251 set: 1. organic-aerosol mixing thermodynamics, *Atmos. Chem. Phys.*, 11, 3303–3318,
1252 <https://doi.org/10.5194/acp-11-3303-2011>, 2011.
- 1253 Epstein, S. A., Riipinen, I., and Donahue, N. M.: A Semiempirical Correlation between Enthalpy of
1254 Vaporization and Saturation Concentration for Organic Aerosol, *Environ. Sci. Technol.*, 44, 743–748,
1255 <https://doi.org/10.1021/es902497z>, 2010.

- 1256 Forster, P., Storelvmo, T., Armour, K., Collins, W., Dufresne, J.-L., Frame, D., Lunt, D. J., Mauritsen,
1257 T., Palmer, M. D., Watanabe, M., Wild, M., and Zhang, H.: The Earth's energy budget, climate
1258 feedbacks, and climate sensitivity, in: *Climate Change 2021: The Physical Science Basis*.
1259 Contribution of Working Group I to the Sixth Assessment Report of the Intergovernmental Panel on
1260 Climate Change, edited by: Masson-Delmotte, V., Zhai, P., Pirani, A., Connors, S. L., Péan, C.,
1261 Berger, S., Caud, N., Chen, Y., Goldfarb, L., Gomis, M. I., Huang, M., Leitzell, K., Lonnoy, E.,
1262 Matthews, J. B. R., Maycock, T. K., Waterfield, T., Yelekçi, Ö., Yu, R., and Zhou, B., Cambridge
1263 University Press, 2021.
- 1264 Fredenslund, A., Jones, R. L., and Prausnitz, J. M.: Group-contribution estimation of activity
1265 coefficients in nonideal liquid mixtures, *AIChE Journal*, 21, 1086–1099,
1266 <https://doi.org/10.1002/aic.690210607>, 1975.
- 1267 Galloway, J. N., Likens, G. E., Keene, W. C., and Miller, J. M.: The composition of precipitation in
1268 remote areas of the world, *Journal of Geophysical Research: Oceans*, 87, 8771–8786,
1269 <https://doi.org/10.1029/JC087iC11p08771>, 1982.
- 1270 Graham, E. L., Wu, C., Bell, D. M., Bertrand, A., Haslett, S. L., Baltensperger, U., El Haddad, I.,
1271 Krejci, R., Riipinen, I., and Mohr, C.: Volatility of aerosol particles from NO₃ oxidation of various
1272 biogenic organic precursors, *EGU sphere*, 1–22, <https://doi.org/10.5194/egusphere-2022-1043>, 2022.
- 1273 Guenther, A., Hewitt, C. N., Erickson, D., Fall, R., Geron, C., Graedel, T., Harley, P., Klinger, L.,
1274 Lerdau, M., McKay, W. A., Pierce, T., Scholes, B., Steinbrecher, R., Tallamraju, R., Taylor, J., and
1275 Zimmerman, P.: A global model of natural volatile organic compound emissions, *Journal of*
1276 *Geophysical Research: Atmospheres*, 100, 8873–8892, <https://doi.org/10.1029/94JD02950>, 1995.
- 1277 Guenther, A. B., Zimmerman, P. R., Harley, P. C., Monson, R. K., and Fall, R.: Isoprene and
1278 monoterpene emission rate variability: Model evaluations and sensitivity analyses, *Journal of*
1279 *Geophysical Research: Atmospheres*, 98, 12609–12617, <https://doi.org/10.1029/93JD00527>, 1993.
- 1280 Gunthe, S. S., Liu, P., Panda, U., Raj, S. S., Sharma, A., Darbyshire, E., Reyes-Villegas, E., Allan, J.,
1281 Chen, Y., Wang, X., Song, S., Pöhlker, M. L., Shi, L., Wang, Y., Kommula, S. M., Liu, T., Ravikrishna,
1282 R., McFiggans, G., Mickley, L. J., Martin, S. T., Pöschl, U., Andreae, M. O., and Coe, H.: Enhanced
1283 aerosol particle growth sustained by high continental chlorine emission in India, *Nat. Geosci.*, 14, 77–
1284 84, <https://doi.org/10.1038/s41561-020-00677-x>, 2021.
- 1285 Hakola, H., Hellén, H., Hemmilä, M., Rinne, J., and Kulmala, M.: In situ measurements of volatile
1286 organic compounds in a boreal forest, *Atmos. Chem. Phys.*, 12, 11665–11678,
1287 <https://doi.org/10.5194/acp-12-11665-2012>, 2012.
- 1288 Hallquist, M., Wenger, J. C., Baltensperger, U., Rudich, Y., Simpson, D., Claeys, M., Dommen, J.,
1289 Donahue, N. M., George, C., Goldstein, A. H., Hamilton, J. F., Herrmann, H., Hoffmann, T., Iinuma,
1290 Y., Jang, M., Jenkin, M. E., Jimenez, J. L., Kiendler-Scharr, A., Maenhaut, W., McFiggans, G., Mentel,
1291 T. F., Monod, A., Prévôt, A. S. H., Seinfeld, J. H., Surratt, J. D., Szmigielski, R., and Wildt, J.: The
1292 formation, properties and impact of secondary organic aerosol: current and emerging issues,
1293 *Atmospheric Chemistry and Physics*, 9, 5155–5236, <https://doi.org/10.5194/acp-9-5155-2009>, 2009.
- 1294 Hänel, G.: The role of aerosol properties during the condensational stage of cloud: A reinvestigation
1295 of numerics and microphysics, *Beitr. Phys. Atmos.*, 60, 321–339, 1987.
- 1296 Hari, P. and Kulmala, M.: Station for Measuring Ecosystem–Atmosphere Relations (SMEAR II),
1297 *Boreal Environ. Res.*, 10, 8, 2005.
- 1298 Hegg, D. A.: Impact of gas-phase HNO₃ and NH₃ on microphysical processes in atmospheric clouds,
1299 *Geophysical Research Letters*, 27, 2201–2204, <https://doi.org/10.1029/1999GL011252>, 2000.
- 1300 Heikkinen, L., Äijälä, M., Riva, M., Luoma, K., Daellenbach, K., Aalto, J., Aalto, P., Aliaga, D., Aurela,
1301 M., Keskinen, H., Makkonen, U., Rantala, P., Kulmala, M., Petäjä, T., Worsnop, D., and Ehn, M.:
1302 Long-term sub-micrometer aerosol chemical composition in the boreal forest: inter- and intra-annual
1303 variability, *Atmos. Chem. Phys.*, 20, 3151–3180, <https://doi.org/10.5194/acp-20-3151-2020>, 2020.

- 1304 Heikkinen, L., Äijälä, M., Daellenbach, K. R., Chen, G., Garmash, O., Aliaga, D., Graeffe, F., Rätty, M.,
 1305 Luoma, K., Aalto, P., Kulmala, M., Petäjä, T., Worsnop, D., and Ehn, M.: Eight years of sub-
 1306 micrometre organic aerosol composition data from the boreal forest characterized using a machine-
 1307 learning approach, *Atmos. Chem. Phys.*, 21, 10081–10109, [https://doi.org/10.5194/acp-21-10081-](https://doi.org/10.5194/acp-21-10081-2021)
 1308 2021, 2021.
- 1309 Hong, J., Häkkinen, S. a. K., Paramonov, M., Äijälä, M., Hakala, J., Nieminen, T., Mikkilä, J., Prisle, N.
 1310 L., Kulmala, M., Riipinen, I., Bilde, M., Kerminen, V.-M., and Petäjä, T.: Hygroscopicity, CCN and
 1311 volatility properties of submicron atmospheric aerosol in a boreal forest environment during the
 1312 summer of 2010, *Atmospheric Chemistry and Physics*, 14, 4733–4748, [https://doi.org/10.5194/acp-](https://doi.org/10.5194/acp-14-4733-2014)
 1313 14-4733-2014, 2014.
- 1314 Hoppel, W. A. and Frick, G. M.: Submicron aerosol size distributions measured over the tropical and
 1315 South Pacific, *Atmospheric Environment. Part A. General Topics*, 24, 645–659,
 1316 [https://doi.org/10.1016/0960-1686\(90\)90020-N](https://doi.org/10.1016/0960-1686(90)90020-N), 1990.
- 1317 Hu, D., Topping, D., and McFiggans, G.: Measured particle water uptake enhanced by co-condensing
 1318 vapours, *Atmospheric Chemistry and Physics*, 18, 14925–14937, [https://doi.org/10.5194/acp-18-](https://doi.org/10.5194/acp-18-14925-2018)
 1319 14925-2018, 2018.
- 1320 Huang, W., Li, H., Sarnela, N., Heikkinen, L., Tham, Y. J., Mikkilä, J., Thomas, S. J., Donahue, N. M.,
 1321 Kulmala, M., and Bianchi, F.: Measurement report: Molecular composition and volatility of gaseous
 1322 organic compounds in a boreal forest – from volatile organic compounds to highly oxygenated organic
 1323 molecules, *Atmos. Chem. Phys.*, 21, 8961–8977, <https://doi.org/10.5194/acp-21-8961-2021>, 2021.
- 1324 Huffman, J. A., Docherty, K. S., Aiken, A. C., Cubison, M. J., Ulbrich, I. M., DeCarlo, P. F., Sueper, D.,
 1325 Jayne, J. T., Worsnop, D. R., Ziemann, P. J., and Jimenez, J. L.: Chemically-resolved aerosol
 1326 volatility measurements from two megacity field studies, *Atmos. Chem. Phys.*, 9, 7161–7182,
 1327 <https://doi.org/10.5194/acp-9-7161-2009>, 2009a.
- 1328 Huffman, J. A., Docherty, K. S., Mohr, C., Cubison, M. J., Ulbrich, I. M., Ziemann, P. J., Onasch, T. B.,
 1329 and Jimenez, J. L.: Chemically-Resolved Volatility Measurements of Organic Aerosol from Different
 1330 Sources, *Environ. Sci. Technol.*, 43, 5351–5357, <https://doi.org/10.1021/es803539d>, 2009b.
- 1331 Hunter, J. F., Day, D. A., Palm, B. B., Yatavelli, R. L. N., Chan, A. W. H., Kaser, L., Cappellin, L.,
 1332 Hayes, P. L., Cross, E. S., Carrasquillo, A. J., Campuzano-Jost, P., Stark, H., Zhao, Y., Hohaus, T.,
 1333 Smith, J. N., Hansel, A., Karl, T., Goldstein, A. H., Guenther, A., Worsnop, D. R., Thornton, J. A.,
 1334 Heald, C. L., Jimenez, J. L., and Kroll, J. H.: Comprehensive characterization of atmospheric organic
 1335 carbon at a forested site, *Nature Geosci.*, 10, 748–753, <https://doi.org/10.1038/ngeo3018>, 2017.
- 1336 Hussein, T., Maso, M. D., Petäjä, T., Koponen, I. K., Paatero, P., Aalto, P. P., Hämeri, K., and
 1337 Kulmala, M.: Evaluation of an automatic algorithm for fitting the particle number size distributions,
 1338 *Boreal Environ. Res.*, 10, 19, 2005.
- 1339 Isaacman-VanWertz, G. and Aumont, B.: Impact of organic molecular structure on the estimation of
 1340 atmospherically relevant physicochemical parameters, *Atmos. Chem. Phys.*, 21, 6541–6563,
 1341 <https://doi.org/10.5194/acp-21-6541-2021>, 2021.
- 1342 Kakavas, S., Pandis, S. N., and Nenes, A.: ISORROPIA-Lite: A Comprehensive Atmospheric Aerosol
 1343 Thermodynamics Module for Earth System Models, *Tellus B: Chemical and Physical Meteorology*, 74,
 1344 1–23, <https://doi.org/10.16993/tellusb.33>, 2022.
- 1345 Kerminen, V.-M., Chen, X., Vakkari, V., Petäjä, T., Kulmala, M., and Bianchi, F.: Atmospheric new
 1346 particle formation and growth: review of field observations, *Environ. Res. Lett.*, 13, 103003,
 1347 <https://doi.org/10.1088/1748-9326/aadf3c>, 2018.
- 1348 Kim, P., Partridge, D. G., and Haywood, J.: Constraining the model representation of the aerosol life
 1349 cycle in relation to sources and sinks, *EGU General Assembly 2020*, Online, 4–8 May 2020,
 1350 EGU2020-21948, <https://doi.org/10.5194/egusphere-egu2020-21948>, 2020.

- 1351 Köhler, H.: The nucleus in and the growth of hygroscopic droplets, *Trans. Faraday Soc.*, 32, 1152–
1352 1161, <https://doi.org/10.1039/TF9363201152>, 1936.
- 1353 Kontkanen, J., Paasonen, P., Aalto, J., Bäck, J., Rantala, P., Petäjä, T., and Kulmala, M.: Simple
1354 proxies for estimating the concentrations of monoterpenes and their oxidation products at a boreal
1355 forest site, *Atmospheric Chemistry and Physics*, 16, 13291–13307, [https://doi.org/10.5194/acp-16-](https://doi.org/10.5194/acp-16-13291-2016)
1356 13291-2016, 2016.
- 1357 Korhonen, P., Kulmala, M., and Vesala, T.: Model simulation of the amount of soluble mass during
1358 cloud droplet formation, *Atmospheric Environment*, 30, 1773–1785, [https://doi.org/10.1016/1352-](https://doi.org/10.1016/1352-2310(95)00380-0)
1359 2310(95)00380-0, 1996.
- 1360 Kulmala, M., Laaksonen, A., Korhonen, P., Vesala, T., Ahonen, T., and Barrett, J. C.: The effect of
1361 atmospheric nitric acid vapor on cloud condensation nucleus activation, *Journal of Geophysical*
1362 *Research: Atmospheres*, 98, 22949–22958, <https://doi.org/10.1029/93JD02070>, 1993.
- 1363 Kulmala, M., Rannik, Ü., Pirjola, L., Maso, M. D., Karimäki, J., Asmi, A., Jäppinen, A., Karhu, V.,
1364 Korhonen, H., Malvikko, S.-P., Puustinen, A., Raittila, J., Romakkaniemi, S., Suni, T., Yli-Koivisto, S.,
1365 Paatero, J., Hari, P., and Vesala, T.: Characterization of atmospheric trace gas and aerosol
1366 concentrations at forest sites in southern and northern Finland using back trajectories, *Boreal Environ.*
1367 *Res.*, 5, 22, 2000.
- 1368 Kulmala, M., Suni, T., Lehtinen, K. E. J., Dal Maso, M., Boy, M., Reissell, A., Rannik, Ü., Aalto, P.,
1369 Keronen, P., Hakola, H., Bäck, J., Hoffmann, T., Vesala, T., and Hari, P.: A new feedback mechanism
1370 linking forests, aerosols, and climate, *Atmospheric Chemistry and Physics*, 4, 557–562,
1371 <https://doi.org/10.5194/acp-4-557-2004>, 2004.
- 1372 Kulmala, M., Nieminen, T., Nikandrova, A., Lehtipalo, K., Manninen, H. E., Kajos, M. K., Kolari, P.,
1373 Lauri, A., Petäjä, T., Krejci, R., Hansson, H.-C., Swietlicki, E., Lindroth, A., Christensen, T. R., Arneth,
1374 A., Hari, P., Bäck, J., Vesala, T., and Kerminen, V.-M.: CO₂-induced terrestrial climate feedback
1375 mechanism: From carbon sink to aerosol source and back, *Boreal Environ. Res.*, 19, 10, 2014.
- 1376 Kyrö, E.-M., Väänänen, R., Kerminen, V.-M., Virkkula, A., Petäjä, T., Asmi, A., Dal Maso, M.,
1377 Nieminen, T., Juhola, S., Shcherbinin, A., Riipinen, I., Lehtipalo, K., Keronen, P., Aalto, P. P., Hari, P.,
1378 and Kulmala, M.: Trends in new particle formation in eastern Lapland, Finland: effect of decreasing
1379 sulfur emissions from Kola Peninsula, *Atmos. Chem. Phys.*, 14, 4383–4396,
1380 <https://doi.org/10.5194/acp-14-4383-2014>, 2014.
- 1381 Lee, B. H., Lopez-Hilfiker, F. D., D'Ambro, E. L., Zhou, P., Boy, M., Petäjä, T., Hao, L., Virtanen, A.,
1382 and Thornton, J. A.: Semi-volatile and highly oxygenated gaseous and particulate organic compounds
1383 observed above a boreal forest canopy, *Atmos. Chem. Phys.*, 18, 11547–11562,
1384 <https://doi.org/10.5194/acp-18-11547-2018>, 2018.
- 1385 Lee, B. H., D'Ambro, E. L., Lopez-Hilfiker, F. D., Schobesberger, S., Mohr, C., Zawadowicz, M. A.,
1386 Liu, J., Shilling, J. E., Hu, W., Palm, B. B., Jimenez, J. L., Hao, L., Virtanen, A., Zhang, H., Goldstein,
1387 A. H., Pye, H. O. T., and Thornton, J. A.: Resolving Ambient Organic Aerosol Formation and Aging
1388 Pathways with Simultaneous Molecular Composition and Volatility Observations, *ACS Earth Space*
1389 *Chem.*, 4, 391–402, <https://doi.org/10.1021/acsearthspacechem.9b00302>, 2020.
- 1390 Lee, I.-Y. and Pruppacher, H. R.: A comparative study on the growth of cloud drops by condensation
1391 using an air parcel model with and without entrainment, *PAGEOPH*, 115, 523–545,
1392 <https://doi.org/10.1007/BF00876119>, 1977.
- 1393 Li, Y., Pöschl, U., and Shiraiwa, M.: Molecular corridors and parameterizations of volatility in the
1394 chemical evolution of organic aerosols, *Atmos. Chem. Phys.*, 16, 3327–3344,
1395 <https://doi.org/10.5194/acp-16-3327-2016>, 2016.
- 1396 Lohmann, U. and Feichter, J.: Global indirect aerosol effects: a review, *Atmos. Chem. Phys.*, 23,
1397 2005.

- 1398 Lopez-Hilfiker, F. D., Mohr, C., Ehn, M., Rubach, F., Kleist, E., Wildt, J., Mentel, T. F., Lutz, A.,
 1399 Hallquist, M., Worsnop, D., and Thornton, J. A.: A novel method for online analysis of gas and particle
 1400 composition: description and evaluation of a Filter Inlet for Gases and AEROSols (FIGAERO), *Atmos.*
 1401 *Meas. Tech.*, 7, 983–1001, <https://doi.org/10.5194/amt-7-983-2014>, 2014.
- 1402 Lopez-Hilfiker, F. D., Mohr, C., Ehn, M., Rubach, F., Kleist, E., Wildt, J., Mentel, T. F., Carrasquillo, A.
 1403 J., Daumit, K. E., Hunter, J. F., Kroll, J. H., Worsnop, D. R., and Thornton, J. A.: Phase partitioning
 1404 and volatility of secondary organic aerosol components formed from α -pinene ozonolysis and OH
 1405 oxidation: the importance of accretion products and other low volatility compounds, *Atmospheric*
 1406 *Chemistry and Physics*, 15, 7765–7776, <https://doi.org/10.5194/acp-15-7765-2015>, 2015.
- 1407 Lowe, S. J.: Modelling the effects of organic aerosol phase partitioning processes on cloud formation,
 1408 PhD thesis, Stockholm University, Faculty of Science, Department of Environmental Science,
 1409 Stockholm, Sweden, 2020.
- 1410 Lowe, S. J., Partridge, D. G., Davies, J. F., Wilson, K. R., Topping, D., and Riipinen, I.: Key drivers of
 1411 cloud response to surface-active organics, *Nat Commun*, 10, 5214, [https://doi.org/10.1038/s41467-](https://doi.org/10.1038/s41467-019-12982-0)
 1412 [019-12982-0](https://doi.org/10.1038/s41467-019-12982-0), 2019.
- 1413 Luoma, K.: AEROSOL OPTICAL PROPERTIES, BLACK CARBON AND THEIR SPATIO-TEMPORAL
 1414 VARIATION, PhD thesis, University of Helsinki, 2021.
- 1415 Lutz, A., Mohr, C., Le Breton, M., Lopez-Hilfiker, F. D., Priestley, M., Thornton, J. A., and Hallquist,
 1416 M.: Gas to Particle Partitioning of Organic Acids in the Boreal Atmosphere, *ACS Earth Space Chem.*,
 1417 3, 1279–1287, <https://doi.org/10.1021/acsearthspacechem.9b00041>, 2019.
- 1418 Mann, G. W., Carslaw, K. S., Spracklen, D. V., Ridley, D. A., Manktelow, P. T., Chipperfield, M. P.,
 1419 Pickering, S. J., and Johnson, C. E.: Description and evaluation of GLOMAP-mode: a modal global
 1420 aerosol microphysics model for the UKCA composition-climate model, *Geoscientific Model*
 1421 *Development*, 3, 519–551, <https://doi.org/10.5194/gmd-3-519-2010>, 2010.
- 1422 Mikhailov, E. F., Mironova, S., Mironov, G., Vlasenko, S., Panov, A., Chi, X., Walter, D., Carbone, S.,
 1423 Artaxo, P., Heimann, M., Lavric, J., Pöschl, U., and Andreae, M. O.: Long-term measurements (2010–
 1424 2014) of carbonaceous aerosol and carbon monoxide at the Zotino Tall Tower Observatory (ZOTTO)
 1425 in central Siberia, *Atmos. Chem. Phys.*, 17, 14365–14392, [https://doi.org/10.5194/acp-17-14365-](https://doi.org/10.5194/acp-17-14365-2017)
 1426 [2017](https://doi.org/10.5194/acp-17-14365-2017), 2017.
- 1427 Millet, D. B., Baasandorj, M., Farmer, D. K., Thornton, J. A., Baumann, K., Brophy, P., Chaliyakunnel,
 1428 S., de Gouw, J. A., Graus, M., Hu, L., Koss, A., Lee, B. H., Lopez-Hilfiker, F. D., Neuman, J. A.,
 1429 Paulot, F., Peischl, J., Pollack, I. B., Ryerson, T. B., Warneke, C., Williams, B. J., and Xu, J.: A large
 1430 and ubiquitous source of atmospheric formic acid, *Atmos. Chem. Phys.*, 15, 6283–6304,
 1431 <https://doi.org/10.5194/acp-15-6283-2015>, 2015.
- 1432 Mohr, C., Lopez-Hilfiker, F. D., Yli-Juuti, T., Heitto, A., Lutz, A., Hallquist, M., D'Ambro, E. L.,
 1433 Rissanen, M. P., Hao, L., Schobesberger, S., Kulmala, M., Mauldin III, R. L., Makkonen, U., Sipilä, M.,
 1434 Petäjä, T., and Thornton, J. A.: Ambient observations of dimers from terpene oxidation in the gas
 1435 phase: Implications for new particle formation and growth, *Geophysical Research Letters*, 44, 2958–
 1436 2966, <https://doi.org/10.1002/2017GL072718>, 2017.
- 1437 Mohr, C., Thornton, J. A., Heitto, A., Lopez-Hilfiker, F. D., Lutz, A., Riipinen, I., Hong, J., Donahue, N.
 1438 M., Hallquist, M., Petäjä, T., Kulmala, M., and Yli-Juuti, T.: Molecular identification of organic vapors
 1439 driving atmospheric nanoparticle growth, *Nat Commun*, 10, 4442, [https://doi.org/10.1038/s41467-019-](https://doi.org/10.1038/s41467-019-12473-2)
 1440 [12473-2](https://doi.org/10.1038/s41467-019-12473-2), 2019.
- 1441 Mulcahy, J. P., Jones, C., Sellar, A., Johnson, B., Boutle, I. A., Jones, A., Andrews, T., Rumbold, S.
 1442 T., Mollard, J., Bellouin, N., Johnson, C. E., Williams, K. D., Grosvenor, D. P., and McCoy, D. T.:
 1443 Improved Aerosol Processes and Effective Radiative Forcing in HadGEM3 and UKESM1, *Journal of*
 1444 *Advances in Modeling Earth Systems*, 10, 2786–2805, <https://doi.org/10.1029/2018MS001464>, 2018.

- 1445 Mulcahy, J. P., Johnson, C., Jones, C. G., Povey, A. C., Scott, C. E., Sellar, A., Turnock, S. T.,
 1446 Woodhouse, M. T., Abraham, N. L., Andrews, M. B., Bellouin, N., Browse, J., Carslaw, K. S., Dalvi,
 1447 M., Folberth, G. A., Glover, M., Grosvenor, D. P., Hardacre, C., Hill, R., Johnson, B., Jones, A.,
 1448 Kipling, Z., Mann, G., Mollard, J., O'Connor, F. M., Palmiéri, J., Reddington, C., Rumbold, S. T.,
 1449 Richardson, M., Schutgens, N. A. J., Stier, P., Stringer, M., Tang, Y., Walton, J., Woodward, S., and
 1450 Yool, A.: Description and evaluation of aerosol in UKESM1 and HadGEM3-GC3.1 CMIP6 historical
 1451 simulations, *Geosci. Model Dev.*, 13, 6383–6423, <https://doi.org/10.5194/gmd-13-6383-2020>, 2020.
- 1452 Murphy, B. N., Julin, J., Riipinen, I., and Ekman, A. M. L.: Organic aerosol processing in tropical deep
 1453 convective clouds: Development of a new model (CRM-ORG) and implications for sources of particle
 1454 number, *Journal of Geophysical Research: Atmospheres*, 120, 10,441–10,464,
 1455 <https://doi.org/10.1002/2015JD023551>, 2015.
- 1456 Ng, N. L., Herndon, S. C., Trimborn, A., Canagaratna, M. R., Croteau, P. L., Onasch, T. B., Sueper,
 1457 D., Worsnop, D. R., Zhang, Q., Sun, Y. L., and Jayne, J. T.: An Aerosol Chemical Speciation Monitor
 1458 (ACSM) for Routine Monitoring of the Composition and Mass Concentrations of Ambient Aerosol,
 1459 *Aerosol Science and Technology*, 45, 780–794, <https://doi.org/10.1080/02786826.2011.560211>,
 1460 2011.
- 1461 Nieminen, T., Asmi, A., Maso, M. D., Aalto, P. P., Keronen, P., Petäjä, T., Kulmala, M., and Kerminen,
 1462 V.-M.: Trends in atmospheric new-particle formation: 16 years of observations in a boreal-forest
 1463 environment, *Boreal Environ. Res.*, 19, 191–214, 2014.
- 1464 NIST Chemistry WebBook: <https://webbook.nist.gov/cgi/cbook.cgi?ID=C64186&Mask=4>, last access:
 1465 8 November 2022.
- 1466 Ovadnevaite, J., Zuend, A., Laaksonen, A., Sanchez, K. J., Roberts, G., Ceburnis, D., Decesari, S.,
 1467 Rinaldi, M., Hodas, N., Facchini, M. C., Seinfeld, J. H., and O'Dowd, C.: Surface tension prevails over
 1468 solute effect in organic-influenced cloud droplet activation, *Nature*, 546, 637–641,
 1469 <https://doi.org/10.1038/nature22806>, 2017.
- 1470 Paasonen, P., Asmi, A., Petäjä, T., Kajos, M. K., Äijälä, M., Junninen, H., Holst, T., Abbatt, J. P. D.,
 1471 Arneth, A., Birmili, W., van der Gon, H. D., Hamed, A., Hoffer, A., Laakso, L., Laaksonen, A., Richard
 1472 Leitch, W., Plass-Dülmer, C., Pryor, S. C., Räisänen, P., Swietlicki, E., Wiedensohler, A., Worsnop,
 1473 D. R., Kerminen, V.-M., and Kulmala, M.: Warming-induced increase in aerosol number concentration
 1474 likely to moderate climate change, *Nature Geosci.*, 6, 438–442, <https://doi.org/10.1038/ngeo1800>,
 1475 2013.
- 1476 Pankow, J. F., Seinfeld, J. H., Asher, W. E., and Erdakos, G. B.: Modeling the Formation of
 1477 Secondary Organic Aerosol. 1. Application of Theoretical Principles to Measurements Obtained in the
 1478 α -Pinene/, β -Pinene/, Sabinene/, Δ 3-Carene/, and Cyclohexene/Ozone Systems, *Environ. Sci.*
 1479 *Technol.*, 35, 1164–1172, <https://doi.org/10.1021/es001321d>, 2001.
- 1480 Paramonov, M., Aalto, P. P., Asmi, A., Prisle, N., Kerminen, V.-M., Kulmala, M., and Petäjä, T.: The
 1481 analysis of size-segregated cloud condensation nuclei counter (CCNC) data and its implications for
 1482 cloud droplet activation, *Atmos. Chem. Phys.*, 13, 10285–10301, [https://doi.org/10.5194/acp-13-](https://doi.org/10.5194/acp-13-10285-2013)
 1483 [10285-2013](https://doi.org/10.5194/acp-13-10285-2013), 2013.
- 1484 Paramonov, M., Kerminen, V.-M., Gysel, M., Aalto, P. P., Andreae, M. O., Asmi, E., Baltensperger, U.,
 1485 Bougiatioti, A., Brus, D., Frank, G. P., Good, N., Gunthe, S. S., Hao, L., Irwin, M., Jaatinen, A.,
 1486 Jurányi, Z., King, S. M., Kortelainen, A., Kristensson, A., Lihavainen, H., Kulmala, M., Lohmann, U.,
 1487 Martin, S. T., McFiggans, G., Mihalopoulos, N., Nenes, A., O'Dowd, C. D., Ovadnevaite, J., Petäjä, T.,
 1488 Pöschl, U., Roberts, G. C., Rose, D., Svenningsson, B., Swietlicki, E., Weingartner, E., Whitehead, J.,
 1489 Wiedensohler, A., Wittbom, C., and Sierau, B.: A synthesis of cloud condensation nuclei counter
 1490 (CCNC) measurements within the EUCAARI network, *Atmospheric Chemistry and Physics*, 15,
 1491 12211–12229, <https://doi.org/10.5194/acp-15-12211-2015>, 2015.
- 1492 Partridge, D., Morales, R., and Stier, P.: Comparing droplet activation parameterisations against
 1493 adiabatic parcel models using a novel inverse modelling framework, *EGU General Assembly*
 1494 *Conference Abstracts*, ADS Bibcode: 2015EGUGA..1714019P, 14019, 2015.

- 1495 Partridge, D. G., Vrugt, J. A., Tunved, P., Ekman, A. M. L., Gorea, D., and Sorooshian, A.: Inverse
1496 modeling of cloud-aerosol interactions – Part 1: Detailed response surface analysis, *Atmos. Chem.*
1497 *Phys.*, 11, 7269–7287, <https://doi.org/10.5194/acp-11-7269-2011>, 2011.
- 1498 Partridge, D. G., Vrugt, J. A., Tunved, P., Ekman, A. M. L., Struthers, H., and Sorooshian, A.: Inverse
1499 modelling of cloud-aerosol interactions – Part 2: Sensitivity tests on liquid phase clouds using a
1500 Markov chain Monte Carlo based simulation approach, *Atmos. Chem. Phys.*, 12, 2823–2847,
1501 <https://doi.org/10.5194/acp-12-2823-2012>, 2012.
- 1502 Peng, Y., Lohmann, U., and Leaitch, R.: Importance of vertical velocity variations in the cloud droplet
1503 nucleation process of marine stratus clouds, *Journal of Geophysical Research: Atmospheres*, 110,
1504 <https://doi.org/10.1029/2004JD004922>, 2005.
- 1505 Petäjä, T., O'Connor, E. J., Moiseev, D., Sinclair, V. A., Manninen, A. J., Väänänen, R., Lerber, A.
1506 von, Thornton, J. A., Nicoll, K., Petersen, W., Chandrasekar, V., Smith, J. N., Winkler, P. M., Krüger,
1507 O., Hakola, H., Timonen, H., Brus, D., Laurila, T., Asmi, E., Riekkola, M.-L., Mona, L., Massoli, P.,
1508 Engelmann, R., Komppula, M., Wang, J., Kuang, C., Bäck, J., Virtanen, A., Levula, J., Ritsche, M.,
1509 and Hickmon, N.: BAEC: A Field Campaign to Elucidate the Impact of Biogenic Aerosols on Clouds
1510 and Climate, *Bulletin of the American Meteorological Society*, 97, 1909–1928,
1511 <https://doi.org/10.1175/BAMS-D-14-00199.1>, 2016.
- 1512 Petäjä, T., Tabakova, K., Manninen, A., Ezhova, E., O'Connor, E., Moiseev, D., Sinclair, V. A.,
1513 Backman, J., Levula, J., Luoma, K., Virkkula, A., Paramonov, M., Rätty, M., Äijälä, M., Heikkinen, L.,
1514 Ehn, M., Sipilä, M., Yli-Juuti, T., Virtanen, A., Ritsche, M., Hickmon, N., Pulik, G., Rosenfeld, D.,
1515 Worsnop, D. R., Bäck, J., Kulmala, M., and Kerminen, V.-M.: Influence of biogenic emissions from
1516 boreal forests on aerosol–cloud interactions, *Nat. Geosci.*, 15, 42–47, <https://doi.org/10.1038/s41561-021-00876-0>, 2022.
- 1518 Petters, M. D. and Kreidenweis, S. M.: A single parameter representation of hygroscopic growth and
1519 cloud condensation nucleus activity – Part 2: Including solubility, *Atmos. Chem. Phys.*, 7, 2008.
- 1520 Pruppacher, H. R. and Klett, J. D.: *Microphysics of Clouds and Precipitation*, Springer Netherlands,
1521 Dordrecht, <https://doi.org/10.1007/978-0-306-48100-0>, 1997.
- 1522 Ridley, J. K., Blockley, E. W., Keen, A. B., Rae, J. G. L., West, A. E., and Schroeder, D.: The sea ice
1523 model component of HadGEM3-GC3.1, *Geoscientific Model Development*, 11, 713–723,
1524 <https://doi.org/10.5194/gmd-11-713-2018>, 2018.
- 1525 Roelofs, G. J. H.: Drop size dependent sulfate distribution in a growing cloud, *J Atmos Chem*, 14,
1526 109–118, <https://doi.org/10.1007/BF00115227>, 1992a.
- 1527 Roelofs, G. J. H.: On the drop and aerosol size dependence of aqueous sulfate formation in a
1528 continental cumulus cloud, *Atmospheric Environment. Part A. General Topics*, 26, 2309–2321,
1529 [https://doi.org/10.1016/0960-1686\(92\)90362-O](https://doi.org/10.1016/0960-1686(92)90362-O), 1992b.
- 1530 Roelofs, G.-J. and Jongen, S.: A model study of the influence of aerosol size and chemical properties
1531 on precipitation formation in warm clouds, *J. Geophys. Res.*, 109,
1532 <https://doi.org/10.1029/2004JD004779>, 2004.
- 1533 Romakkaniemi, S., Kokkola, H., and Laaksonen, A.: Parameterization of the nitric acid effect on CCN
1534 activation, *Atmospheric Chemistry and Physics*, 5, 879–885, <https://doi.org/10.5194/acp-5-879-2005>,
1535 2005.
- 1536 Ruehl, C. R., Chuang, P. Y., Nenes, A., Cappa, C. D., Kolesar, K. R., and Goldstein, A. H.: Strong
1537 evidence of surface tension reduction in microscopic aqueous droplets, *Geophysical Research*
1538 *Letters*, 39, <https://doi.org/10.1029/2012GL053706>, 2012.
- 1539 Ruehl, C. R., Davies, J. F., and Wilson, K. R.: An interfacial mechanism for cloud droplet formation on
1540 organic aerosols, *Science*, 351, 1447–1450, <https://doi.org/10.1126/science.aad4889>, 2016.

- 1541 Schobesberger, S., Lopez-Hilfiker, F. D., Taipale, D., Millet, D. B., D'Ambro, E. L., Rantala, P.,
1542 Mammarella, I., Zhou, P., Wolfe, G. M., Lee, B. H., Boy, M., and Thornton, J. A.: High upward fluxes
1543 of formic acid from a boreal forest canopy, *Geophysical Research Letters*, 43, 9342–9351,
1544 <https://doi.org/10.1002/2016GL069599>, 2016.
- 1545 Scott, C. E., Arnold, S. R., Monks, S. A., Asmi, A., Paasonen, P., and Spracklen, D. V.: Substantial
1546 large-scale feedbacks between natural aerosols and climate, *Nature Geosci*, 11, 44–48,
1547 <https://doi.org/10.1038/s41561-017-0020-5>, 2018.
- 1548 Sellar, A. A., Jones, C. G., Mulcahy, J. P., Tang, Y., Yool, A., Wiltshire, A., O'Connor, F. M., Stringer,
1549 M., Hill, R., Palmieri, J., Woodward, S., de Mora, L., Kuhlbrodt, T., Rumbold, S. T., Kelley, D. I., Ellis,
1550 R., Johnson, C. E., Walton, J., Abraham, N. L., Andrews, M. B., Andrews, T., Archibald, A. T.,
1551 Berthou, S., Burke, E., Blockley, E., Carslaw, K., Dalvi, M., Edwards, J., Folberth, G. A., Gedney, N.,
1552 Griffiths, P. T., Harper, A. B., Hendry, M. A., Hewitt, A. J., Johnson, B., Jones, A., Jones, C. D.,
1553 Keeble, J., Liddicoat, S., Morgenstern, O., Parker, R. J., Predoi, V., Robertson, E., Siahann, A.,
1554 Smith, R. S., Swaminathan, R., Woodhouse, M. T., Zeng, G., and Zerroukat, M.: UKESM1:
1555 Description and Evaluation of the U.K. Earth System Model, *Journal of Advances in Modeling Earth*
1556 *Systems*, 11, 4513–4558, <https://doi.org/10.1029/2019MS001739>, 2019.
- 1557 Sellar, A. A., Walton, J., Jones, C. G., Wood, R., Abraham, N. L., Andrejczuk, M., Andrews, M. B.,
1558 Andrews, T., Archibald, A. T., de Mora, L., Dyson, H., Elkington, M., Ellis, R., Florek, P., Good, P.,
1559 Gohar, L., Haddad, S., Hardiman, S. C., Hogan, E., Iwi, A., Jones, C. D., Johnson, B., Kelley, D. I.,
1560 Kettleborough, J., Knight, J. R., Köhler, M. O., Kuhlbrodt, T., Liddicoat, S., Linova-Pavlova, I.,
1561 Mizielinski, M. S., Morgenstern, O., Mulcahy, J., Neining, E., O'Connor, F. M., Petrie, R., Ridley, J.,
1562 Rioual, J.-C., Roberts, M., Robertson, E., Rumbold, S., Seddon, J., Shepherd, H., Shim, S.,
1563 Stephens, A., Teixeira, J. C., Tang, Y., Williams, J., Wiltshire, A., and Griffiths, P. T.: Implementation
1564 of U.K. Earth System Models for CMIP6, *Journal of Advances in Modeling Earth Systems*, 12,
1565 e2019MS001946, <https://doi.org/10.1029/2019MS001946>, 2020.
- 1566 Shrivastava, M., Cappa, C. D., Fan, J., Goldstein, A. H., Guenther, A. B., Jimenez, J. L., Kuang, C.,
1567 Laskin, A., Martin, S. T., Ng, N. L., Petaja, T., Pierce, J. R., Rasch, P. J., Roldin, P., Seinfeld, J. H.,
1568 Shilling, J., Smith, J. N., Thornton, J. A., Volkamer, R., Wang, J., Worsnop, D. R., Zaveri, R. A.,
1569 Zelenyuk, A., and Zhang, Q.: Recent advances in understanding secondary organic aerosol:
1570 Implications for global climate forcing, *Reviews of Geophysics*, 55, 509–559,
1571 <https://doi.org/10.1002/2016RG000540>, 2017.
- 1572 Sihto, S.-L., Mikkilä, J., Vanhanen, J., Ehn, M., Liao, L., Lehtipalo, K., Aalto, P. P., Duplissy, J.,
1573 Petäjä, T., Kerminen, V.-M., Boy, M., and Kulmala, M.: Seasonal variation of CCN concentrations and
1574 aerosol activation properties in boreal forest, *Atmospheric Chemistry and Physics*, 11, 13269–13285,
1575 <https://doi.org/10.5194/acp-11-13269-2011>, 2011.
- 1576 Simpson, E., Connolly, P., and McFiggans, G.: An investigation into the performance of four cloud
1577 droplet activation parameterisations, *Geoscientific Model Development*, 7, 1535–1542,
1578 <https://doi.org/10.5194/gmd-7-1535-2014>, 2014.
- 1579 Sporre, M. K., Blichner, S. M., Karset, I. H. H., Makkonen, R., and Berntsen, T. K.: BVOC–aerosol–
1580 climate feedbacks investigated using NorESM, *Atmospheric Chemistry and Physics*, 19, 4763–4782,
1581 <https://doi.org/10.5194/acp-19-4763-2019>, 2019.
- 1582 Sporre, M. K., Blichner, S. M., Schrödner, R., Karset, I. H. H., Berntsen, T. K., van Noije, T., Bergman,
1583 T., O'Donnell, D., and Makkonen, R.: Large difference in aerosol radiative effects from BVOC-SOA
1584 treatment in three Earth system models, *Atmospheric Chemistry and Physics*, 20, 8953–8973,
1585 <https://doi.org/10.5194/acp-20-8953-2020>, 2020.
- 1586 Spracklen, D. V., Bonn, B., and Carslaw, K. S.: Boreal forests, aerosols and the impacts on clouds
1587 and climate, *Philosophical Transactions of the Royal Society A: Mathematical, Physical and*
1588 *Engineering Sciences*, 366, 4613–4626, <https://doi.org/10.1098/rsta.2008.0201>, 2008.
- 1589 Storkey, D., Blaker, A. T., Mathiot, P., Megann, A., Aksenov, Y., Blockley, E. W., Calvert, D., Graham,
1590 T., Hewitt, H. T., Hyder, P., Kuhlbrodt, T., Rae, J. G. L., and Sinha, B.: UK Global Ocean GO6 and

- 1591 GO7: a traceable hierarchy of model resolutions, *Geoscientific Model Development*, 11, 3187–3213,
1592 <https://doi.org/10.5194/gmd-11-3187-2018>, 2018.
- 1593 Thornhill, G., Collins, W., Olivie, D., Skeie, R. B., Archibald, A., Bauer, S., Checa-Garcia, R., Fiedler,
1594 S., Folberth, G., Gjernundsen, A., Horowitz, L., Lamarque, J.-F., Michou, M., Mulcahy, J., Nabat, P.,
1595 Naik, V., O'Connor, F. M., Paulot, F., Schulz, M., Scott, C. E., Seférian, R., Smith, C., Takemura, T.,
1596 Tilmes, S., Tsigaridis, K., and Weber, J.: Climate-driven chemistry and aerosol feedbacks in CMIP6
1597 Earth system models, *Atmospheric Chemistry and Physics*, 21, 1105–1126,
1598 <https://doi.org/10.5194/acp-21-1105-2021>, 2021.
- 1599 Thornton, J. A., Mohr, C., Schobesberger, S., D'Ambro, E. L., Lee, B. H., and Lopez-Hilfiker, F. D.:
1600 Evaluating Organic Aerosol Sources and Evolution with a Combined Molecular Composition and
1601 Volatility Framework Using the Filter Inlet for Gases and Aerosols (FIGAERO), *Acc. Chem. Res.*, 53,
1602 1415–1426, <https://doi.org/10.1021/acs.accounts.0c00259>, 2020.
- 1603 Topping, D., Connolly, P., and McFiggans, G.: Cloud droplet number enhanced by co-condensation of
1604 organic vapours, *Nature Geosci*, 6, 443–446, <https://doi.org/10.1038/ngeo1809>, 2013.
- 1605 Topping, D. O. and McFiggans, G.: Tight coupling of particle size, number and composition in
1606 atmospheric cloud droplet activation, *Atmospheric Chemistry and Physics*, 12, 3253–3260,
1607 <https://doi.org/10.5194/acp-12-3253-2012>, 2012.
- 1608 Tunved, P., Hansson, H.-C., Kerminen, V.-M., Ström, J., Maso, M. D., Lihavainen, H., Viisanen, Y.,
1609 Aalto, P. P., Komppula, M., and Kulmala, M.: High Natural Aerosol Loading over Boreal Forests,
1610 *Science*, 312, 261–263, <https://doi.org/10.1126/science.1123052>, 2006.
- 1611 Turnock, S. T., Allen, R. J., Andrews, M., Bauer, S. E., Deushi, M., Emmons, L., Good, P., Horowitz,
1612 L., John, J. G., Michou, M., Nabat, P., Naik, V., Neubauer, D., O'Connor, F. M., Olivie, D., Oshima, N.,
1613 Schulz, M., Sellar, A., Shim, S., Takemura, T., Tilmes, S., Tsigaridis, K., Wu, T., and Zhang, J.:
1614 Historical and future changes in air pollutants from CMIP6 models, *Atmospheric Chemistry and
1615 Physics*, 20, 14547–14579, <https://doi.org/10.5194/acp-20-14547-2020>, 2020.
- 1616 Twomey, S.: Pollution and the planetary albedo, *Atmospheric Environment (1967)*, 8, 1251–1256,
1617 [https://doi.org/10.1016/0004-6981\(74\)90004-3](https://doi.org/10.1016/0004-6981(74)90004-3), 1974.
- 1618 Twomey, S.: The Influence of Pollution on the Shortwave Albedo of Clouds, *Journal of the
1619 Atmospheric Sciences*, 34, 1149–1152, [https://doi.org/10.1175/1520-0469\(1977\)034<1149:TIOPO>2.0.CO;2](https://doi.org/10.1175/1520-0469(1977)034<1149:TIOPO>2.0.CO;2), 1977.
- 1621 Vehkamäki, H., Kulmala, M., Napari, I., Lehtinen, K. E. J., Timmreck, C., Noppel, M., and Laaksonen,
1622 A.: An improved parameterization for sulfuric acid–water nucleation rates for tropospheric and
1623 stratospheric conditions, *Journal of Geophysical Research: Atmospheres*, 107, AAC 3-1-AAC 3-10,
1624 <https://doi.org/10.1029/2002JD002184>, 2002.
- 1625 Walters, D., Boutle, I., Brooks, M., Melvin, T., Stratton, R., Vosper, S., Wells, H., Williams, K., Wood,
1626 N., Allen, T., Bushell, A., Copsey, D., Earnshaw, P., Edwards, J., Gross, M., Hardiman, S., Harris, C.,
1627 Heming, J., Klingaman, N., Levine, R., Manners, J., Martin, G., Milton, S., Mittermaier, M., Morcrette,
1628 C., Riddick, T., Roberts, M., Sanchez, C., Selwood, P., Stirling, A., Smith, C., Suri, D., Tennant, W.,
1629 Vidale, P. L., Wilkinson, J., Willett, M., Woolnough, S., and Xavier, P.: The Met Office Unified Model
1630 Global Atmosphere 6.0/6.1 and JULES Global Land 6.0/6.1 configurations, *Geoscientific Model
1631 Development*, 10, 1487–1520, <https://doi.org/10.5194/gmd-10-1487-2017>, 2017.
- 1632 Wang, Y., Chen, Y., Wu, Z., Shang, D., Bian, Y., Du, Z., Schmitt, S. H., Su, R., Gkatzelis, G. I.,
1633 Schlag, P., Hohaus, T., Voliotis, A., Lu, K., Zeng, L., Zhao, C., Alfarra, M. R., McFiggans, G.,
1634 Wiedensohler, A., Kiendler-Scharr, A., Zhang, Y., and Hu, M.: Mutual promotion between aerosol
1635 particle liquid water and particulate nitrate enhancement leads to severe nitrate-dominated particulate
1636 matter pollution and low visibility, *Atmospheric Chemistry and Physics*, 20, 2161–2175,
1637 <https://doi.org/10.5194/acp-20-2161-2020>, 2020.

- 1638 West, R. E. L., Stier, P., Jones, A., Johnson, C. E., Mann, G. W., Bellouin, N., Partridge, D. G., and
1639 Kipling, Z.: The importance of vertical velocity variability for estimates of the indirect aerosol effects,
1640 *Atmos. Chem. Phys.*, 14, 6369–6393, <https://doi.org/10.5194/acp-14-6369-2014>, 2014.
- 1641 Williams, J., Crowley, J., Fischer, H., Harder, H., Martinez, M., Petäjä, T., Rinne, J., Bäck, J., Boy, M.,
1642 Dal Maso, M., Hakala, J., Kajos, M., Keronen, P., Rantala, P., Aalto, J., Aaltonen, H., Paatero, J.,
1643 Vesala, T., Hakola, H., Levula, J., Pohja, T., Herrmann, F., Auld, J., Mesarchaki, E., Song, W.,
1644 Yassaa, N., Nölscher, A., Johnson, A. M., Custer, T., Sinha, V., Thieser, J., Pouvesle, N., Taraborrelli,
1645 D., Tang, M. J., Bozem, H., Hosaynali-Beygi, Z., Axinte, R., Oswald, R., Novelli, A., Kubistin, D.,
1646 Hens, K., Javed, U., Trawny, K., Breitenberger, C., Hidalgo, P. J., Ebben, C. J., Geiger, F. M.,
1647 Corrigan, A. L., Russell, L. M., Ouwersloot, H. G., Vilà-Guerau de Arellano, J., Ganzeveld, L., Vogel,
1648 A., Beck, M., Bayerle, A., Kampf, C. J., Bertelmann, M., Köllner, F., Hoffmann, T., Valverde, J.,
1649 González, D., Riekkola, M.-L., Kulmala, M., and Lelieveld, J.: The summertime Boreal forest field
1650 measurement intensive (HUMPPA-COPEC-2010): an overview of meteorological and chemical
1651 influences, *Atmos. Chem. Phys.*, 11, 10599–10618, <https://doi.org/10.5194/acp-11-10599-2011>, 2011.
- 1652 Yan, C., Nie, W., Äijälä, M., Rissanen, M. P., Canagaratna, M. R., Massoli, P., Junninen, H., Jokinen,
1653 T., Sarnela, N., Häme, S. A. K., Schobesberger, S., Canonaco, F., Yao, L., Prévôt, A. S. H., Petäjä,
1654 T., Kulmala, M., Sipilä, M., Worsnop, D. R., and Ehn, M.: Source characterization of highly oxidized
1655 multifunctional compounds in a boreal forest environment using positive matrix factorization, *Atmos.*
1656 *Chem. Phys.*, 16, 12715–12731, <https://doi.org/10.5194/acp-16-12715-2016>, 2016.
- 1657 Yatavelli, R. L. N., Mohr, C., Stark, H., Day, D. A., Thompson, S. L., Lopez-Hilfiker, F. D.,
1658 Campuzano-Jost, P., Palm, B. B., Vogel, A. L., Hoffmann, T., Heikkinen, L., Äijälä, M., Ng, N. L.,
1659 Kimmel, J. R., Canagaratna, M. R., Ehn, M., Junninen, H., Cubison, M. J., Petäjä, T., Kulmala, M.,
1660 Jayne, J. T., Worsnop, D. R., and Jimenez, J. L.: Estimating the contribution of organic acids to
1661 northern hemispheric continental organic aerosol, *Geophysical Research Letters*, 42, 6084–6090,
1662 <https://doi.org/10.1002/2015GL064650>, 2015.
- 1663 Yli-Juuti, T., Mielonen, T., Heikkinen, L., Arola, A., Ehn, M., Isokääntä, S., Keskinen, H.-M., Kulmala,
1664 M., Laakso, A., Lipponen, A., Luoma, K., Mikkonen, S., Nieminen, T., Paasonen, P., Petäjä, T.,
1665 Romakkaniemi, S., Tonttila, J., Kokkola, H., and Virtanen, A.: Significance of the organic aerosol
1666 driven climate feedback in the boreal area, *Nat Commun*, 12, 5637, [https://doi.org/10.1038/s41467-](https://doi.org/10.1038/s41467-021-25850-7)
1667 021-25850-7, 2021.
- 1668 Ylivinkka, I., Kaupinmäki, S., Virman, M., Peltola, M., Taipale, D., Petäjä, T., Kerminen, V.-M.,
1669 Kulmala, M., and Ezhova, E.: Clouds over Hyytiälä, Finland: an algorithm to classify clouds based on
1670 solar radiation and cloud base height measurements, *Atmospheric Measurement Techniques*, 13,
1671 5595–5619, <https://doi.org/10.5194/amt-13-5595-2020>, 2020.
- 1672 Zhang, Y., Peräkylä, O., Yan, C., Heikkinen, L., Äijälä, M., Daellenbach, K. R., Zha, Q., Riva, M.,
1673 Garmash, O., Junninen, H., Paatero, P., Worsnop, D., and Ehn, M.: Insights into atmospheric
1674 oxidation processes by performing factor analyses on subranges of mass spectra, *Atmos. Chem.*
1675 *Phys.*, 20, 5945–5961, <https://doi.org/10.5194/acp-20-5945-2020>, 2020.
- 1676